Identifying regulatory and spatial genomic architectural elements using cell type independent machine and deep learning models

Laura D. Martens [1], Oisin Faust [1], Liviu Pirvan [1], Dora Bihary [1], Shamith A. Samarajiwa [1*]

[1]MRC Cancer Unit, Hutchison-MRC Research Centre, Cambridge Biomedical Campus, University of Cambridge, Cambridge, CB2 0XZ, UK.
* Corresponding author email address: ss861@mrc-cu.cam.ac.uk

Abstract

Chromosomal conformation capture methods such as Hi-C enables mapping of genome-wide chromatin interactions and is a promising technology to understand the role of spatial chromatin organisation in gene regulation. However, the generation and analysis of these data sets at high resolutions remain technically challenging and costly. We developed a machine and deep learning approach to predict functionally important, highly interacting chromatin regions (HICR) and topologically associated domain (TAD) boundaries independent of Hi-C data in both normal physiological states and pathological conditions such as cancer. This approach utilises gradient boosted trees and convolutional neural networks trained on both Hi-C and histone modification epigenomic data from three different cell types. Given only epigenomic modification data these models are able to predict chromatin interactions and TAD boundaries with high accuracy. We demonstrate that our models are transferable across cell types, indicating that combinatorial histone mark signatures may be universal predictors for highly interacting chromatin regions and spatial chromatin architecture elements.

Introduction

Interactions between cis-acting regulatory elements and trans-acting regulatory proteins are facilitated by spatial genome organisation, chromatin accessibility, epigenetic modifications and non-coding RNA interactions that contribute to the complexity of gene regulatory programmes. Our genetic material, in the form of nuclear DNA is organised into chromosomes, with each DNA molecule wrapped up and compressed into super-coiled material known as chromatin. Various studies have demonstrated that this packaging is not merely useful to compact the DNA but also plays an important role in gene regulation. [1, 2, 3]. At the simplest level, DNA is wrapped around nucleosomes forming a beads on a string structure. These nucleosomes are made of two copies each of H2A, H2B, H3 and H4 histone proteins with 146 nucleotides of DNA wrapped around each nucleosome in 1.67 superhelical left handed turns [4]. Each nucleosome is connected to each other by short linker DNA associated with linker histone H1. The N-terminal tails of these histone proteins can be post-translationally modified, with more than 80 modifications "histone marks" identified so far [5, 6, 7]. These modifications act in a yet to be deciphered combinatorial code. However, the association of some of these modifications in forming active or inactive states as well as condensed heterochromatin or accessible euchromatin are known [8].

Chromatin forms both global [9] and local three dimensional architectures; an example being the looping of DNA to bring distal regulatory regions such as enhancer and promoter into

close spatial proximity [10, 11, 12, 13, 14]. More recently, chromosomal conformation capture (3C) methods such as 4C [15], 5C [16] and Hi-C [17] as well as immunoprecipitation based ChIA-PET [18] have provided insight into genome scale chromatin interactions and spatial genomic organisation [19]. Analysis of Hi-C data revealed the general hierarchical organisation of chromatin, which includes structures such as A/B compartments [20], topologically associated domains (TADs) [21, 22], and long-distance chromatin loops [23].

TADs are rosette like nested structures formed by localised chromatin interaction regions in the 0.2-1.0 Mb range. Their main characteristic is the preferential interactions of TAD enclosed chromatin regions with each other. This feature is distinctly recognisable in Hi-C contact maps as patterns of interacting loci along the diagonal. It has been proposed that TADs have an insulating function that facilitates inter–domain interaction of regulatory elements while restricting most of the cross–boundary enhancer promoter interactions (EPIs) [22, 24]. However, more recent studies show that some EPIs can form intra–TAD interactions by escaping TAD boundary insulation [25, 26]. Evidence for the role of TADs in gene regulation is seen in both normal physiological as well as pathogenic situations. Some of these include co-regulated genes that share the same TAD [27] and clusters of enhancer-promoter interactions observed within TADs [28]. The CCCTC-binding factor (CTCF) has many functions, one of which is to act as an insulator that prevents enhancer-promoter interactions. CTCF also contributes to loop formation and is enriched at certain TAD-boundaries. The disruption of CTCF binding sites present in TAD boundaries through DNA hypermethylation lead to ectopic transcription via interactions across TAD boundaries in cancer [29].

Furthermore, it has been shown that many TAD boundaries are conserved across cell types, with only a small subset of boundaries being cell type specific [24, 30]. TAD boundary regions often coincide with histone modifications associated with regions of gene transcriptional activity, with active enhancer-promoter associated histone modifications such as tri-methylation of Lysines on Histone H3 (H3K4me3 and H3K36me3) and the localisation of essential (housekeeping) genes [23, 24]. They are also usually marked by CTCF and cohesin, chromatin loop forming proteins [22, 24, 31, 32]. CTCF and cohesin were proposed to promote the extrusion of loops, which contributes to TAD formation [33, 34]. According to this model, cohesin extrudes chromatin outwards until it meets barriers in the form of CTCF [33, 34, 35]. Interestingly, the termination of extrusion through CTCF seems to be dependent on the orientation of the protein, as they appear predominantly in convergent orientation [23, 36]. In a Hi-C contact map, these loops anchored at CTCF binding sites correspond to intense, highly localised signals. Although the extrusion model is not yet completely experimentally tested, there is strong evidence supporting it. For example, changes in the orientation of CTCF can change and disrupt chromatin loops and TADs [34, 36]. Furthermore, chromatin loops and TADs are globally lost or reduced upon depletion of cohesin [37, 38, 39].

Chromatin interactions, loops, TADs and A/B compartments can be identified using Hi-C based approaches. Specialised versions of the assay such as promoter capture Hi-C (cHi-C) can detect targeted enhancer-promoter interactions, as well as interaction at the single cell level using single cell Hi-C (scHi-C). These methods need considerable technical expertise, are time consuming and costly. It has also been estimated that to capture all chromatin interactions in a cell population at least 5-10 billion reads are needed. While recent advances in sequencing technologies make this possible, it is far too expensive to carry out these deep Hi-C experiments. In the last five years machine and deep learning technologies have provided revolutionary solutions to many difficult problems in biomedicine [40]. Their utility in genomics [41], biomedical image classification [42], protein structure prediction [43] and many clinical applications [44, 45, 46] have been demonstrated. In this study we investigate the possibility of using combinatorial

histone modification patterns, detected with machine and deep learning approaches to identify both spatial and functional chromatin interactions and architectures.

Methods

Cell-lines and data sets

Chromosomal conformation capture (Hi-C) and histone modification ChIP-seq data were obtained for three different cell types. These included IMR90, a human fetal diploid lung fibroblast cell line; K562, a human chronic myelogenous leukemia cell line; and GM12878, a human B-lymphocyte cell line. All different data processing steps are visualized by the workflow in Figure S8.

Histone mark data

ChIP-seq data processing ChIP-seq data was downloaded from the Roadmap Epigenome project [47] and included fold-enrichment and p-values for all available histone modifications (see Table S3) for the three cell types in this study. CTCF binding profiles for all three cell types were obtained from ChIP-seq experiments with accession numbers, denoted in Table 1. ChIP-seq reads were mapped to the human reference genome (hg19) using the *BWA aligner (version 0.7.12)* [48]. Low-quality reads (mapping quality <20) as well as known adapter contamination were trimmed using *Cutadapt (version 1.10.0)* [49], and reads mapping to the 'blacklisted' regions identified by ENCODE [50] were further removed. Average fragment size was determined using the *ChIPQC* Bioconductor package [51], and peak calling was performed with *MACS2 (version 2.1.0)* [52], using fragment size as an extension size (–extsize) parameter.

Table 1. Cell type, accession number and number of reads of all CTCF ChIP-seq data sets used.

cell type	Dataset	Accession number	Number of reads
IMR90	Replicate 1	SRR639078	8,913,904
	Replicate 2	SRR639079	12,556,107
GM12878	Replicate 1	SRR227594	29,883,393
	Replicate 2	SRR227595	17,949,455
	Replicate 3	SRR299277	16,990,693
	Replicate 4	SRR299312	14,311,175
	Replicate 5	SRR299314	31,495,220
	Replicate 6	SRR357519	8,420,728
	Replicate 7	SRR357520	16,281,148
	Replicate 8	SRR502628	29,485,157
	Replicate 9	SRR502629	16,411,438
	Replicate 10	SRR585830	21,319,387
K562	Replicate 1	SRR227523	19,656,110
	Replicate 2	SRR227524	16,448,282
	Replicate 3	SRR299298	32,740,518
	Replicate 4	SRR299327	18,123,856
	Replicate5	SRR299341	27,953,212
	Replicate 6	SRR577849	24,638,860
	Replicate 6	SRR577850	31,332,287

When computing signal in a given genomic interval, fold-enrichment values were set to zero where the corresponding p-value was greater than 0.01. The remaining values were binned by

taking the mean over a distance of 200 base pairs. We chose this bin size since it is approximately the length of DNA wrapped around a typical nucleosome [53] inclusive of the linker DNA. We then applied an arcsine transformation to the data and divided the resulting data by their mean. The data transformations were carried out to ensure that values were close to 1, since it has been empirically found that neural networks work better with input values close to 1 [54].

Hi-C data sets

Hi-C data were obtained in the form of unprocessed (paired-end Illumina reads) fastq files for IMR90 cells from the NCBI Gene Expression Omnibus (GEO)- accession GSE43070[12]. The data set consisted of six biological replicates that were merged for downstream analysis. For K562 and GM12878, the data was obtained from [23], from NCBI GEO, with accession: GSE63525. Due to the size of the files, not all biological replicates were downloaded but only the largest files. Accession numbers are denoted in Table 2.

Table 2. Cell type, accession number and number of reads of all Hi-C datasets used.

cell type	Dataset	Accession number	Number of reads
IMR90	Replicate 1	SRX212172	397,194,480
	Replicate 2	SRX212173	440,242,130
	Replicate 3	SRX294948	621,089,009
	Replicate 4	SRX294949	529,157,703
	Replicate 5	SRX294950	234,133,577
	Replicate 6	SRX294951	208,710,657
GM12878	Replicate 1	SRX764940	304,049,399
	Replicate 2	SRX764958	322,202,135
	Replicate 3	SRX764960	347,956,701
K562	Replicate 1	SRX765004	456,757,799
	Replicate 2	SRX765005	591,854,553
	Replicate 3	SRX765006	79,905,895
	Replicate 4	SRX765007	79,578,049

Generation of Hi-C interaction maps Interaction maps for each data set were generated using *Hi-C-Pro (version 2.11.1)* [55]. The pipeline used the *Bowtie2 (version 2.3.5)* aligner [56] and reads were mapped to the hg19 reference genome, containing chromosomes 1-22 and X. The *in silico* restriction fragment maps were generated for IMR90 using the restriction enzyme *HindIII* whereas maps for the other two cell lines were generated using *MBoI*. The interaction matrices were generated for different bin sizes (chromatin anchors): 20000, 40000, 80000, 150000, 500000 and 1000000 bps. This was necessary since different architectures can be detected at different length scales. We used a bins with 20000 bp resolution for HICRs detection and 40000 bp for TADs.

Normalisation of Hi-C interaction maps The interaction matrices were normalised using ICE (iterative correction and eigenvector decomposition) method to eliminate systematic biases [57]. The ICE method was applied within the *Hi-C-Pro* pipeline using the python package *iced (version 0.5.1)*.

Significant interactions detection We used *FitHiC (version 1.3.0, Bioconductor)* [58], a tool for assessing statistical significance of chromosomal contacts with respect to a background, to

obtain a list of significant interactions. The original source code of *FitHiC* was altered to consider the whole chromosome interaction matrices. *FitHiC* returns a p-value and a multiple testing corrected q-value for each interaction. The default parameters were used when running *FitHiC*. Based on the significant chromatin interaction, we ranked the chromatin anchors according to their interaction frequency. In more detail, we defined significant interactions as those with a q-value below 0.05. Then, for each bin, we summed up the total number of interactions with other bins, weighted by the respective interaction frequency.

TAD boundary detection *TADbit (version 0.4.28)* [59] was used to call TADs. *TADbit* analyses the contact distribution along the genome and subsequently segments it into TADs. To calculate the position of borders between TADs along a chromosome, *TADbit* employs a breakpoint detection algorithm [60]. TADs were called on interaction matrices of 40 kb resolution. TAD boundaries were defined as either the start or end of a TAD, as long as the *TADbit* scores of both TADs surrounding it were greater than 5. This ensured, that TADs were only called when they spanned more than three bins since smaller regions cannot reliably be called with the breakpoint detection algorithm. To create a balanced training set, we randomly chose non-boundaries, equal to the number of TAD boundaries.

Identifying biological significance of HICRs and TADs Functional enrichment analysis of the HICRs was performed using *GREAT (version 3.0.0)* [61]. Overlaps of HICRs and TAD boundaries was calculated and visualized using the R package *ComplexHeatmaps (version 2.3.3)* [62]. TAD boundaries associated with CTCF were identified by selecting those with a CTCF ChIP-seq peak within +/- 20 kb of the boundary using *BEDTools (version 2.18* [63]. The 20 kb window was chosen because this reflects the inherent uncertainty in the exact position of the domain calls due to 40 kb binning.

Machine Learning Approaches

All learning tasks were designed as binary classification tasks with labels $y = 1$ for positive examples and $y = 0$ for negative examples. The aim was to predict if histone marks in a given region classified as a HICR or not, TAD boundary or non TAD boundary. We applied the following three supervised machine learning techniques in training to detect HICRs and TAD boundaries and compared them. We used the same training and test set for all three models with a train-test split of 0.8-0.2. All models were implemented in Python *(version 3.7.5)*. Bayesian hyper-parameter optimisation maximising the mean accuracy on the validation set (5-fold cross validation) was performed using the Python package *hyperopt (version 0.1.2)* [64]. Hyperparameter spaces of all three models can be found in the Supplementary Data, Tables S4 - S6. Predictions were generated on the test set after refitting on the training set.

Gradient boosted ensemble of decision trees The gradient boosting library *XGBoost (version 0.90)* was used for model fitting [65]. The mean over the histone mark signal adjacent to HICRs and TAD boundaries was used as input features. Since the signal for HICRs was very localized, we restricted the region to the extent of the HICR (here 20 kb). For TAD boundaries, we extended the region of the actual TAD boundary (40 kb) on both sides to a total length spanning 200 kb.

Logistic regression The class SGDClassifier from the *scikit-learn library (version 0.21.2)* [66] was used for model fitting. The strength of the regularization parameter and solver were selected by maximizing the accuracy with 5-fold cross-validation. Input features were the same as for XGBoost.

Convolutional Neural Network model A convolutional neural network was constructed in *Keras (version 2.2.4)* with *Tensorflow (version 1.14.0)* as back-end. Here, we did not average the input signal, but used each bin in a window of 200 kb around HICRs and TAD boundaries as one input node to the network. An overview of the architectures can be found in Fig. S9. One convolution block consisted of a convolution layer, batch normalisation before the ReLU activation and a max pooling layer. Before entering the fully connected network, we applied dropout. The final classification was done using a sigmoid activation function with a threshold of 0.5. For training, we used the Adam learning algorithm [67] with cross-entropy loss.

Feature importance The importance of individual features was measured using mean absolute SHAP values (*shap (version 0.32.1)*) of predictions made on the training set.

Performance Evaluation Classification performance of each task is evaluated by the area under the precision-recall curve (PR-AUC) and receiver operating characteristics curve (ROC-AUC). Additionally, we reported accuracy, recall, precision and F1 (harmonic mean of precision and recall) for each task.

Results

Overview

Three very different cell lines were used in our analyses; these included GM12878 transformed B lymphocytes, K567 myelogenous leukaemia cells and IMR90 diploid fetal fibroblasts. Fig. 1 gives an overview of the methodology used. Features were extracted from ChIP-seq derived histone modification data and Hi-C based chromatin interaction data. Details of the data sets, data cleaning, processing and feature extraction is described in Methods. Fold-enrichment values and p-values for all available histone markers and CCCTC-binding factor (CTCF) binding profiles were obtained for all three cell types, see Table S3 for a detailed list. Signal regions binned by aggregating over a distance of 200 base pairs were used to extract features (Fig. 1a). We chose this bin size since it is approximately the length of DNA wrapped around a nucleosome [53] plus its linker DNA.

Similarly, chromatin interactions were extracted from ICE normalised interaction matrices from Hi-C data (Fig1b). TAD boundaries were called using these matrices and statistically significant boundaries were identified. Highly Interacting Chromatin Regions (HICR) were identified. A balanced training set was defined for TAD boundaries and HICRs targets from normalized Hi-C contact maps for three different cell types – IMR90, GM12878 and K562, Figure 1b. Machine and deep learning approaches were used to create a binary classification model, which classifies a region in the genome as HICR or TAD boundary (labels) from the underlying histone mark signal (features). The process of label and feature creation and model training is illustrated in Fig. 1c–g.

Properties of HICR, TAD boundary targets and histone mark features

Defining highly interacting chromatin regions (HICR). HICRs were defined by significant interactions from the iced-normalized interaction count matrix, identified by *FitHiC* [58], Fig. 1b. For each chromatin anchor, we counted the number of statistically significant interactions, which showed a similar long tailed distribution in all three cell types (Fig. 2a for GM12878 and Fig. S1a–b for IMR90 and K562 respectively). Across all three cell types, 30% of all anchors showed a high significant interaction frequency, with the remaining 70% showing very few interactions. Interestingly, although the distributions were similar, the frequency differed between cell types. While for K562, the top 10% interacting regions showed more than 3700

interactions per loci, IMR90 cells showed a minimum of 890 interactions, while GM12878 cells showed an intermediate value of around 1700 interactions. The differences here could be both technical (the IMR90 Hi-C data set has lower resolution) or biological in origin.

Over-representation Analysis To determine if HICRs either have a role in maintaining chromatin spatial structure or a functional role in transcriptional regulation or both we investigated the relevance of these highly interacting anchors. The enrichment of these regions for biologically significant genomic elements or annotation were explored. We divided the set into two, the top 10% and top 30% to top 10%. Since they formed the set of most interacting genomic regions of each cell type, we scrutinised these regions for their contribution to cell-specific gene regulation.

Functional enrichment analysis using GREAT[61] provided insights into the biological functions of the highly interacting chromatin regions. Indeed, genes nearby the anchors in the top set were significantly enriched for cell type-specific processes (Fig. 2b and Fig. S1c–d). Chromatin anchors of the IMR90 cell line, a human fetal lung cell line, were enriched for developmental processes related to the mesodermal origin of lung fibroblasts, such as mesoderm development (P-value = 5.5×10^{-46}) or positive regulation of angiogenesis (P-value = 4.7×10^{-54}). In GM12878, a B-lymphocyte cell line, terms related to immune response were highly enriched, e.g.positive regulation of immune response (P-value = 2.4×10^{-121}). Leukocyte mediated immunity, as well as response to endoplasmic reticulum stress, were enriched in K562 anchors, from a human chronic myelogenous leukaemia cell line. Endoplasmic reticulum (ER) is an organelle involved in protein folding and assembly, Ca^{2+} homeostasis, and lipid biosynthesis. Multiple stress conditions can trigger ER stress leading to an unfolded protein response and is commonly observed in both acute and chronic myelogenous leukaemia [68]. In the top 30% to top 20% group, we found more general processes, e.g. ribosome binding (P-value = 8.93×10^{-8})) These could be interactions involved in regulating essential cellular processes common between cell types. As a control, we also analysed anchors at the lower end of the distribution, with no significant results for functional enrichment. Since we were interested in investigating cell type specific properties, we defined the top 10% as our highly interacting chromatin regions (HICR). For the set of non-HICRs, we randomly sampled an equal number from the low-interacting anchors.

Histone modification enrichment in HICR flanking regions To explore if histone modification signatures were correlated with HICRs and TAD boundaries, we examined the patterns of histone modifications adjacent to each HICR and TAD boundary. A distinct signal is evident in the histone modifications around the HICRs. For comparison, we illustrate the background signal found in regions that were not identified as HICR in a lighter colour. When multiple histone modifications in 100 bp region flanking HICRs were examined, high enrichment for CTCF (suggesting local loop formation) and activating histone modifications (H3K27ac, H3K4me1, H3K4me3) associated with active enhancer and promoter regions. In addition, transcriptionally active gene body containing (H3K36me3) regions were enriched compared to non-HICR control regions. DNase hypersensitivity assays in GM12878 showed that these active regions were also nucleosome free open regions. Similarly, heterochromatin modifications such as inactivating H3K9me3 and H3K27me3 marks showed very little enrichment compared to non-HICR regions (visualised in a lighter colour) in all three cell lines, however these heterochromatin effects were variable across the cell types with slight enrichment of H3K27me3, associated with facultative repression of promoter rich regions (Fig. 2c and Fig. S2a and b).

TADs are very similar between the three cell types, are enriched for CTCF at boundaries and show little enrichment of most histone modifications. TADs were called using the *TADbit*[59] algorithm. TAD boundaries were defined as either the start or end of a TAD, as long as the *TADbit* scores of both TADs surrounding it were greater than boundary

score of 5. We checked the distribution of sizes of the TADs to see if they were on a reasonable length scale, see Fig. 3a. The size of most TADs was between 0.1 and 1.5 Mb with a mean size of 500 kb, which is in agreement with [23]. A few very large TADs were predicted that could most likely be miscalled boundaries by *TADbit*. We additionally calculated the overlap of the identified TAD boundaries with CTCF peaks. In both cell types, we found that 65-70% of TAD boundaries were associated with CTCF peaks which agrees with findings in [24]. Unlike HICR regions TAD boundaries had very little enrichment of histone modifications, compared to non-TAD regions, the exception being the transcriptionally active gene body associated modification H3K36me3 (Fig3c, Fig. S3a and b).

Fig. 3c and Fig. S3a and b show the spatial pattern of histone marks in a 300 kb around the TAD boundaries. It is striking that compared to that seen in HICRs the signal was a lot weaker and the peaks broader, however, there were some histone modifications that were enriched at TAD boundaries. Most importantly, CTCF, a marker of TAD boundaries, was enriched. Additionally, markers associated with active promoters and genes showed a stronger signal (H3K36me3 in all three cell types and H3K4me3 in IMR90 cells) which is distinctly different to repressive marks that were not enriched or even depleted in boundary regions (H3K9me3 and H3K27me3). Again, this is in agreement with findings that TAD boundaries correlate with histone modifications that are associated with active gene regions and are often marked by the CTCF-biding sites [23].

Overlap between HICRs and TAD boundaries Fig. 3b shows that there is very little overlap between HICRs and TAD boundaries. Only 20-30% of TAD boundary or HICR regions were common to the 3 cell types suggesting that the majority of HICRs and TADs were unique to cell types. While a very small number of HICRs and TADs overlapped within a cell type, there were no between cell-type overlap of these elements.

Binary classification of HICRs and TAD boundaries

We created and evaluated three different model types – logistic regression, gradient boosted decision trees (XGBoost) and a convolutional neural network (CNN). Here we present the results from the XGBoost and the CNN. Logistic regression performed surprisingly well, but overall did not outperform the XGBoost or CNN model (see Table S7 and S8).

XGBoost model. We trained two binary XGBoost models per cell type, one for HICRs and one for TAD boundaries. Each model learnt to classify HICR/TAD boundary vs non-HICR/non-TAD boundary using combinatorial histone mark signatures. As input, we used the mean of the histone mark signal over a certain region adjacent to the HICRs and TAD boundaries, see Fig. 1c–d. We evaluated different window sizes, ranging from 20 kb to 300 kb. For HICRs we found that a very small window of 20 kb produced the best results (which is equivalent to the used Hi-C resolution), TAD boundaries required a broader region of 200 kb. Additionally, we trained the models with all histone marks that were available for the cell type and also with only the consensus set (Table S3) for better comparability of the different combinatorial effects of histone modifications.
The performance of the boosted tree classifier for GM12878 is shown in Fig. 4 using both ROC curves and precision-recall (PR) curves and in Fig. S4 for the other two cell lines. Additional metrics are shown in Table 3 and 4. Overall, there is very good performance across all cell types, with only a small range between the best performing model (ROC-AUC 0.999 and PR-AUC 0.999) and the worst performing model (ROC-AUC 0.981 and PR-AUC 0.977).
Classification of TAD boundaries proved to be more difficult with the best performing model getting a test performance of 0.774 (ROC-AUC) and 0.722 (PR-AUC). One problem here could be the lack of significant histone mark signals adjacent to the TAD boundaries (Fig. 3c) which

makes classification more difficult.
Interestingly, the use of all histone marks compared to the consensus set did not have a huge effect on model performance. The biggest increase in test set performance could be seen for IMR90 which had most histone marks available (27 in total), which indicates that model performance might increase when taking additional histone marks into account that were not available for the two other cell types.

Table 3. HICR: Different metrics for evaluation of XGBoost model.

cell type	markers	Acc.	Recall	Precision	F1	ROC AUC	PR AUC
GM12878	all markers	0.953	0.953	0.950	0.952	0.991	0.990
	consensus	0.949	0.949	0.946	0.947	0.989	0.988
IMR90	all markers	0.950	0.957	0.939	0.948	0.990	0.989
	consensus	0.930	0.933	0.921	0.927	0.981	0.977
K562	all markers	0.987	0.989	0.985	0.987	0.999	0.999
	consensus	0.984	0.985	0.982	0.984	0.998	0.998

Table 4. TAD boundaries: Different metrics for evaluation of XGBoost model.

cell type	markers	Acc.	Recall	Precision	F1	ROC AUC	PR AUC
GM12878	all markers	0.715	0.818	0.670	0.737	0.774	0.722
	consensus	0.706	0.807	0.664	0.728	0.772	0.724
IMR90	all markers	0.704	0.808	0.663	0.728	0.770	0.713
	consensus	0.697	0.790	0.659	0.719	0.762	0.708
K562	all markers	0.707	0.795	0.683	0.735	0.757	0.715
	consensus	0.702	0.796	0.678	0.732	0.757	0.718

Inspection of model features We used SHAP values to get an insight into which histone marks are very predictive for both HICRs and TAD boundaries. In Fig. 4e and f, we list the histone mark features of the HICR model for GM12878 sorted by mean absolute SHAP value and show the distribution across all predictions. Additionally, sample points are coloured according to their feature value. An increased signal of well-known markers for active regulatory elements such as DNase, H3K4me1 and H3K36me3 are strong indicators for the presence of a HICR. On the contrary, higher values of H3K4me3 give lower probability to the positive class. The other two cell types show similar distributions (Fig. S5) with a few striking differences. In IMR90 (Fig. S5a) the acetylation of H2AK5 has highest feature importance, a mark that is linked to active regions [69]. This could also explain the observed increase in performance when using the full model (all markers) compared to only the consensus set. Also, in both IMR90 and K562, a lot more importance is given to the repressive mark H3K27me3, indicating that we might be capturing both active and inactive (facultative heterochromatin) regulatory elements.

Fig. 4f and Fig. S5b and d, show the distribution of SHAP values for the prediction of TAD boundaries. TAD boundaries are often marked by CTCF [24] and its presence has the biggest influence on model prediction in all three cell types. In GM12878, both H3K36me3 and also H3K79me2 that have previously been found to be associated with TAD boundaries [23], also have a high feature importance. Interestingly, H3K4me1 has an anti-correlated relationship with model prediction, indicating that TAD boundaries are depleted for this enhancer associated mark. In IMR90 and K562, H3K9me3 ranks among the top four most important mark with an anti-correlated relationship. In both cases the feature analysis has shown that the models pick

up relationships between the chromatin feature and histone marks that were not apparent by merely looking at the average signal.

Convolutional Neural Network With the aim of creating a more robust model, especially for TAD boundary predictions, we designed two convolutional neural networks, with the idea that it would better capture patterns within the histone mark signal (see Methods and Supplementary Data for the detailed architecture and hyperparameter space). The network was provided with a sequence of binned histone mark data in a window of 200 kb adjacent to HICRs and TAD boundaries.
Fig. 5a–d, Fig. S6 and Tables 5-6 show the performance on the test set. The CNN outperformed the XGBoost model in both classification tasks. For HICRs the mean ROC-AUC was improved from 0.991 to 0.997 and mean PR-AUC from 0.990 to 0.997. For TAD boundaries the model increased the performance from a mean ROC-AUC of 0.765 to 0.784 and average PR-AUC of 0.717 to 0.755. Although the overall performance improved, this was not the case for K562.

Table 5. HICR: Different metrics for evaluation of CNN model.

cell type	markers	Acc.	Recall	Precision	F1	ROC AUC	PR AUC
GM12878	all markers	0.989	0.992	0.984	0.988	0.999	0.999
	consensus	0.981	0.995	0.968	0.981	0.998	0.998
IMR90	all markers	0.978	0.975	0.980	0.977	0.997	0.997
	consensus	0.958	0.971	0.942	0.956	0.988	0.987
K562	all markers	0.995	0.993	0.996	0.995	0.999	0.999
	consensus	0.996	0.996	0.996	0.996	1.000	1.000

Table 6. TAD boundaries: Different metrics for evaluation of CNN model.

cell type	markers	Acc.	Recall	Precision	F1	ROC AUC	PR AUC
GM12878	all markers	0.733	0.797	0.709	0.750	0.803	0.784
	consensus	0.723	0.836	0.684	0.752	0.787	0.765
IMR90	all markers	0.733	0.810	0.706	0.754	0.806	0.776
	consensus	0.725	0.841	0.687	0.756	0.794	0.759
K562	all markers	0.697	0.710	0.693	0.701	0.757	0.722
	consensus	0.694	0.838	0.651	0.733	0.758	0.724

Transfer models to assess model generalisability across cell types We found that CNNs trained on cell type specific data perform better than conventional machine learning models at predicting HICRs and TAD boundaries from histone mark data. Building on that, we examined if that was a phenomenon that could be attributed to the cell type specific training data given to the network or if histone marks adjacent to our targets experienced cell type independent patterns. For this, we tested the performance of a model trained on one cell type and tested on data from a different cell type. Since we did not have all histone marks for every cell type, we compared performance using the consensus set. Fig. 6a–d, Fig. S7 and Tables 7–8 show the evaluations.
Interestingly, the performances are surprisingly good with all AUC values close to the evaluation on the same cell type. Mostly the models just perform 1-2% worse on predicting HICRs and

TAD boundaries in other cell types. However, in the case of predicting TAD boundaries in IMR90 from the model trained on GM12878, the performance significantly decreases. Even though the ROC-AUC and PR-AUC are comparable to testing on the same cell type (ROC-AUC: 0.787 vs. 0.747 and PR-AUC: 0.765 vs. 0.693), we get very low accuracy and F1 score (0.56 and 0.334 respectively). This is mainly due to the very low recall, which means that many TAD boundaries are misclassified as non-TAD boundaries. When looking at the opposite case (predicting TAD boundaries in GM12878 from models trained on IMR90), accuracy is also not very high (0.597).Overall, however, these finding suggest that even though we found that HICRs and TAD boundaries vary across cell types, there might be a more general and cell type invariant pattern of histone modifications, marking these chromatin features.

Table 7. HICR: Different metrics for evaluation of CNN model tested on all three cell types.

cell type trained	cell type tested	Acc.	Recall	Precision	F1	ROC AUC	PR AUC
IMR90	IMR90	0.958	0.971	0.942	0.956	0.988	0.987
	GM12878	0.954	0.928	0.976	0.951	0.989	0.989
	K562	0.952	0.920	0.984	0.951	0.994	0.995
GM12878	IMR90	0.928	0.887	0.959	0.922	0.983	0.982
	GM12878	0.981	0.995	0.968	0.981	0.998	0.998
	K562	0.969	0.946	0.991	0.968	0.993	0.994
K562	IMR90	0.906	0.831	0.969	0.895	0.983	0.982
	GM12878	0.948	0.989	0.911	0.948	0.991	0.989
	K562	0.996	0.996	0.996	0.996	1.000	1.000

Table 8. TAD boundaries: Different metrics for evaluation of CNN model tested on all three cell types.

cell type trained	cell type tested	Acc.	Recall	Precision	F1	ROC AUC	PR AUC
IMR90	IMR90	0.725	0.841	0.687	0.756	0.794	0.759
	GM12878	0.597	0.977	0.557	0.709	0.756	0.739
	K562	0.618	0.934	0.573	0.710	0.738	0.700
GM12878	IMR90	0.560	0.217	0.716	0.334	0.747	0.693
	GM12878	0.723	0.836	0.684	0.752	0.787	0.765
	K562	0.692	0.752	0.673	0.710	0.746	0.726
K562	IMR90	0.681	0.690	0.683	0.687	0.750	0.712
	GM12878	0.670	0.903	0.618	0.734	0.780	0.755
	K562	0.694	0.838	0.651	0.733	0.758	0.724

Discussion

Precise regulatory mechanisms are essential to control gene expression in multicellular organisms with hundreds of different cell types, where dysregulation of gene expression can potentiate pathological disease states. Our understanding of how chromatin interactions and spatial genome organisation contribute to transcriptional regulation has vastly improved due to chromosomal conformation capture methods such as 4C, 5C and various Hi-C methods. Hi-C interaction maps provide a means to understand how transitions in the three-dimensional organization of the genome can affect gene regulation in both normal and disease states [70]. However these methods are technically challenging, time consuming, have many associated biases and are expensive. Altogether, these are a motivating driver for developing computational methods that can predict similar functional interactions and chromatin architectures as those detected by Hi-C using more easily produced epigenetic data. Patterns of epigenomic activity obtained from easily performed ChIP-seq experiments that detect post-translational histone modifications are one such data type. We utilised histone modification data together with machine and deep learning approaches to develop methods to predict chromatin interactions and domains.

We demonstrate that gradient boosted decision trees (XGboost) and deep convolutional neural networks (CNN) could successfully predict two important chromatin topologies – highly interacting chromatin regions (HICRs) and topologically associated domain (TAD) boundaries – from histone modification data in a cell type independent manner. The top 30% of all interactions are high frequency interactions. Gene ontology enrichment of these three cell types demonstrate that the top 10% of interaction regions contain genes involved in cell type specific functions and that 10-30% interaction regions contain genes contributing to general cellular functions. Using Hi-C data from three cell types – IMR90, GM12878 and K562 – we constructed normalized interaction count matrices from which we identified the locations of highly interacting chromatin regions and TAD boundaries as targets of a classification task. The models were subsequently trained on well studied histone modification ChIP-seq data and CTCF insulator binding profiles. Both machine and deep learning approaches demonstrated good test set performance with the CNN yielding better results (mean ROC-AUC 0. in the final evaluation. Whilst we obtained almost perfect test set performance (mean ROC-AUC 0.999 and PR-AUC of 0.999) when predicting HICRs, TAD boundaries proved more difficult to classify (mean ROC-AUC of 0.804 and PR-AUC of 0.784). The use of all histone features compared to just a consensus set made very little difference

In all three cell types, enrichment of both active enhancer (H3K27Ac, H3K4me1), promoter (H3K4me3, H3K4me2), gene body transcriptional activity (H3K36me3) associated histone modification suggests that HICRs are enriched for active enhancer-promoter regions. as well as Furthermore the presence of loop forming CTCF in HICR regions, nucleosome depletion (DNase hypersensitivity), and H4K20me1 which is associated with transcriptional activation in GM12878 and K562), and H2A.Z activity (in GM12878 and K562), which is a histone that when included in nucleosomes proximal to the TSS, correlates with higher gene expression [71] all of which indicates that HICRs are rich in enhancer-promoter regions and actively transcribed genes [69]. While depletion of repressive heterochromatin associated modifications (H3K9me3, H3K27me3) is observed, there is cell type variation. Interestingly in the K562 cancer cells HICR regions, moderately increased activity of the facultative heterochromatic mark H3K27me3 is observed and in GM12878 cells moderately high levels of constitutive heterochromatin mark is seen, suggesting in addition to the active elements, the presence of inactive, poised or primed regulatory elements in these interacting regions. Some of these regions may also form architectural contacts that maintain chromatin structure.

The lower accuracy in predicting TAD boundaries may indicate that factors other than histone

modification might play a role in specification of these boundary regions. The principles of TAD formation are an ongoing field of research and it is believed that there are different classes of TADs with different functionalities. Their role in gene regulation is demonstrated when disruption of certain TAD boundaries causes ectopic chromosomal contacts and long-range transcriptional dysregulation across boundaries [22]. It is believed that these boundaries are associated with transcription [24, 72] or correspond to a division between active and repressed chromatin regions, i.e. similar to the mutually exclusive A and B chromatin compartment organization containing active and inactive domains observed across a larger genomic scale [23, 73]. There is emerging evidence that TADs (and their boundary regions are) may belong to distinct functional classes. Mutations and genetic aberrations in the TAD-spanning WNT6/IHH/EPHA4/PAX3 locus are believed to cause defects in limb development. CRISPR/Cas9 genome editing of the CTCF binding sites containing TAD boundary region resulted in enhancer-promoter "rewiring" leading to ectopic gene expression [74] associated with defects in limb development. Conversely, disruption of TAD boundaries through the removal of all boundary associated CTCF sites at the Sox9-Kcnj2 locus which regulate mouse limb bud development resulted in the fusion of neighbouring TADs but had very little effects on gene expression [75].

As we and others have shown, a high proportion of TAD boundaries (65-90% depending on cell type) are associated with CTCF [24]. However, there is also a significant fraction of TAD boundaries that are CTCF independent and are unaffected by CTCF loss [76]. It is also possible that demarcation of certain TAD boundaries are specified by types of histone modifications or by other genomic features that are currently not well studied . Functional diversity of TADs are exemplified by their involvement as units of replication timing regulation during genome replication, in addition to being architectural units involved in genome organisation [77]. Henderson et al., used deep learning methods to predict TAD boundaries using high resolution Hi-C in Drosophila [78], highlighting the utility of deep neural networks in chromatin biology. Unsurprisingly, There was very little genomic overlap between the HICRs and TAD boundaries identified by our machine and deep learning models. When there was overlap, it was always less than 20% and was detected between the same cell type or the same region types across the three cell types. However there was no overlap between HICRs and TAD boundaries between cell types. While this suggests cell type specificity, it also indicates that DNA regions involved in transcriptional regulation and spatial genomic organisation are distinct, even though detectable using the same collection of epigenetic modifications.

Interpretability and explainability of machine learning models are a desired characteristic. We utilised SHAP (SHapley Additive exPlanations) method developed by Lundberg and Lee to assess contribution of individual predictions [79]. SHAP contributes to understanding interpretability of models and the method is based on the game theoretically optimal Shapley Values. Using SHAP values of the XGBoost models, we investigated the importance of different histone marks for the overall prediction. This identified CTCF and H3K36me3 to have high predictive power for TAD boundaries, which is a well-known association[23]. We hypothesized that our highly interacting and cell type specific chromatin regions could play a role in bringing tissue specific regulatory elements into proximity. Indeed, we found HICRs to be highly conserved evolutionarily, enriched for gene transcription start sites, transcription factor clusters and enhancers (Table S1 and S2). Surprisingly, despite the claim by Huang et al., [80] that in their analysis similar chromatin regions contained a large percentage of super-enhancers, HICRs contained very few super-enhancer regions even though we used a number of different super-enhancer databases (Table S1). (Table S1). The SHAP analysis revealed that the enhancer mark H3K4me1, transcriptional activation mark K4K20me1 and H3K36me3 which defines exons on gene bodies and may be involved in splicing as well as preventing runaway transcription [81, 82, 83]. All these studies suggest HICRs are involved in transcriptional regulation. However, some impor-

tance was also given by SHAP to the presence of H3K27me3, and H3K9me3 modifications representing both facultative and constitutive heterochromatin formation respectively. Previous studies have identified distinct classes of enhancers (e.g. active, inactive, primed, poised), which can be distinguished by specific chromatin signatures [84, 85, 86, 87]. They are marked by H3K4me1, active enhancers are additionally associated with H3K27ac and poised enhancers are distinguishable by being marked with H3K27me3 and not H3K27ac. This suggest HICRs are composed of a heterogeneous collection of active, inactive, poised and primed enhancer regions.

We demonstrated that the deep neural network (CNN) models were cell type independent, with models trained on one cell type that could predict HICRs and TAD boundaries using only histone modifications on the other two cell types, with comparable high-performance to when tested on the cell type of origin. This clearly indicates that certain specific histone modification patterns are associated with both HICRs and TAD boundaries.

Many models and computational approaches have been developed to predict chromatin interactions and topological domain boundaries. These include an eclectic collection of computational methods including TADLactua [88], PCGS [89], nTDP [90] and BART [80]. TADLacuta utilised random forest and deep learning methods and integrated histone modifications, CTCF binding and transcription factor motifs predict TAD boundaries with an AUC ROC accuracy 0.867 [88]. Huang et al., [80] used a statistical approach known as Bayesian Additive Regression Trees (BART) to predict interacting regions or "hubs" and TAD boundaries. They used a 300kb window around signal regions and averaged reads for each histone modification. Their prediction accuracy AUC 0.869 for interactions and 0.774 for TAD boundaries. While models built with averaged cell type data performed well for TAD prediction, cell type specific data was needed for interaction prediction. In their model CTCF was the most important predictor for domain boundaries, H3m4me1 and H3m27me3 were important in interaction prediction. Huang et al., [80] speculate that these combinatorial patterns may be involved in mediating chromatin interactions. However it is also possible that histone modifications merely demarcate regulatory elements that are involved in functional (enhancer-promoter interactions) or structural (spatial genome organization) and are selected by chromatin interacting proteins such as remodelers and transcription factors in forming interactions. This may explain why in our analysis HICRs contain elements with both active and inactive modifications indicating that these potential EPI regions may contain a mixture of active, inactive, poised and primed enhancer and promoter elements. Hong et al., [89] developed population greedy search algorithm (PGSA) to identify boundary enriched motifs and concluded that in addition to CTCF other TF such as ZNF143, ZNF274, YY1, SP1, ZNf274 and chromatin accessibility (DHS) as well as epigenetic modifications H3K36me3, gene associated features and protein complexes such as RNA PolII, TSSs were all enriched at TAD boundaries. Similarly Sefer and Kingsford developed a convex semi-nonparametric approach called nTDP based on Bernstein polynomials to explore the joint effects of histone markers on TAD formation [90].

In conclusion we demonstrated that our machine and deep learning models can predict genomic elements with potential transcriptional and architectural functions (usually detected by 3C methods) from histone modification ChIP-seq data with high accuracy. We also show that the histone signatures demarcating these elements are cell type independent, where models trained on one cell type can be used to identify these elements in other cell types with considerable accuracy.

Data Availability

All code for this project was produced in Python Jupyter or R notebooks and will be made available through GitHub after peer reviewed publication. Bash scripts, R and Python code were appropriately annotated for future usage. Only publicly available data sets were used.

Author Contribution

S.A.S conceived the study. L.D.M carried out the data processing, genomic data analysis and developed the machine learning models. O.F contributed to the initial analysis during a summer studentship. L.P and D.B were involved with data analysis and provided guidance. L.D.M and S.A.S wrote the manuscript with input from the other authors.

Acknowledgements

This work was supported by UK Medical Research Council core funding (MC_UU_12022/10) to S.A.S. L.P is supported by a Medical Research Council Doctoral Training Award. L.D.M., O.P, D.B were supported by MRC core funding. We also thank members of the S.A.S laboratory that read and commented on the manuscript.

Figures

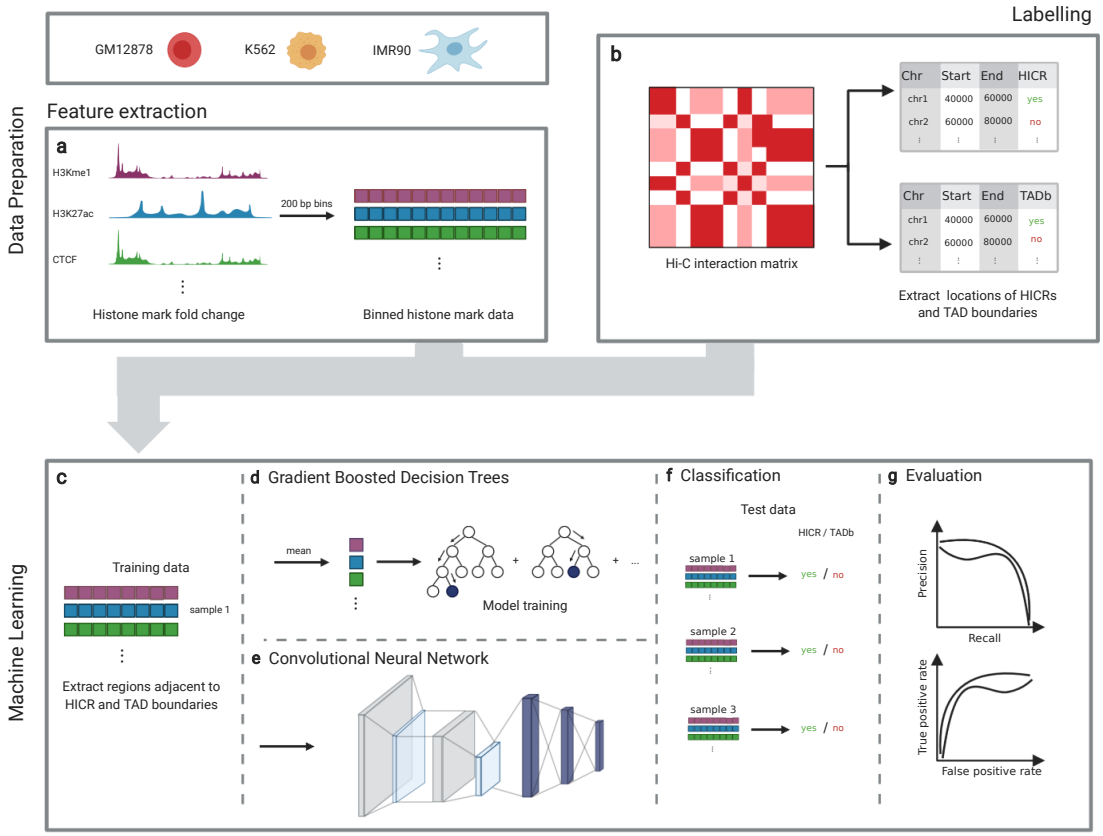

Fig. 1. Overview of workflow All analysis steps were performed for three different cell-types – IMR90, GM12878 and K562. **a-b**, Data Preparation. **a**, For feature creation, fold-change values for all available histone marks were aggregated over 200 bp bins, the typical length of DNA spooled over nucleosomes with linker DNA. **b** As targets, highly interacting chromatin regions (HICRs) and TAD boundaries were extracted from normalized Hi-C interaction matrices. For HICRs, a resolution of 20 kb was used, for TAD boundaries 40 kb. All anchors were then labelled as either HICR or TAD boundary or non-HICR, TAD boundary to construct binary classification task. For training, we sampled a subset of anchors with negative label, to create a balanced set. **c-f**, Machine Learning. **c** For each target (HICR or TAD boundary), bins in a window adjacent to it were extracted. 80% of the data was used for training, with 5-fold cross validation. The remaining 20% were used for the final evaluation. **d,e** A binary classifier to predict HICRs and TAD boundaries was trained on the extracted labels and features. Both gradient-boosted decision trees and convolutional neural networks were evaluated. In the first case, the histone mark signal was averaged to have one feature per histone mark. **f**, Trained models were used to classify the left-out test data. **g**, Evaluation. The models were evaluated on the basis of precision-recall curves and receiver operating characteristics (ROC) curves.

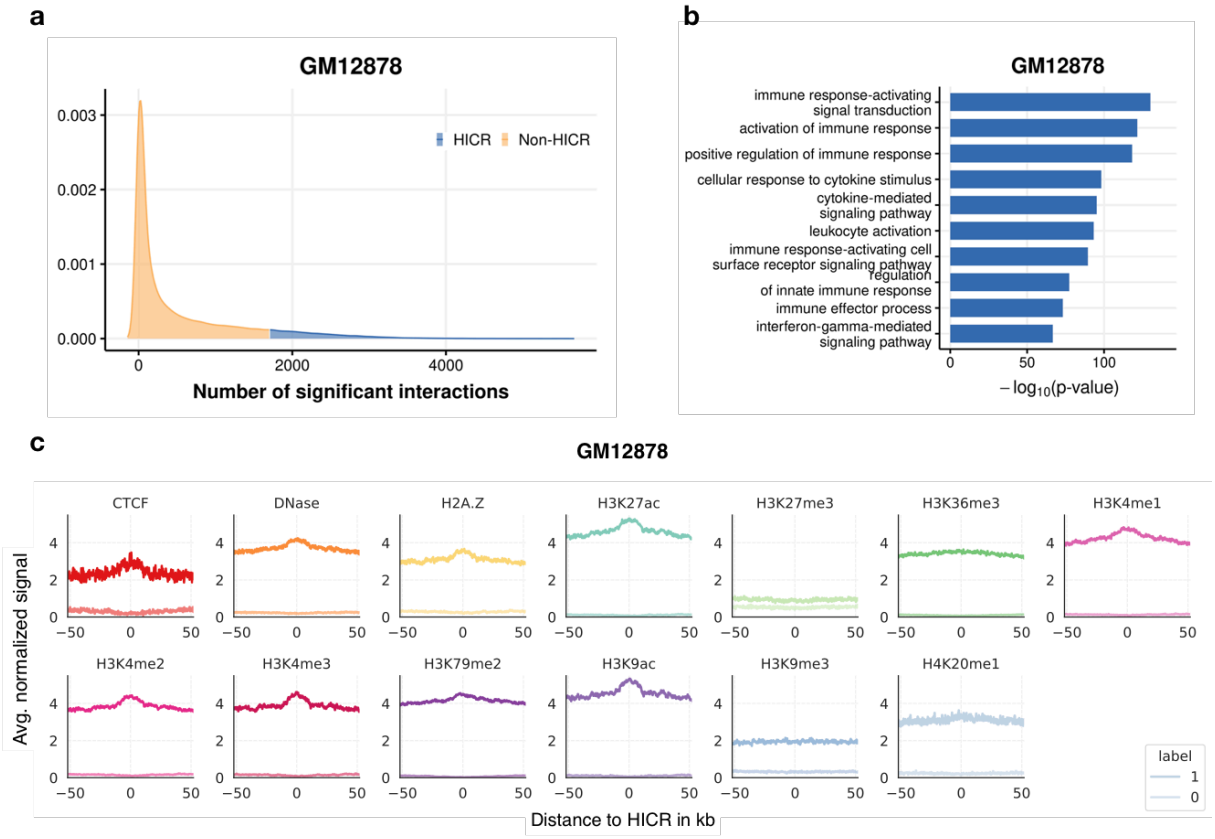

Fig. 2. Inspection of HICRs. a, The distribution of significant counts for the GM12878 cell line. shaded in blue are the top 10% of interactions, which were defined as Highly Interacting Chromatin Regions (HICRs). **b**, Functional enrichment analysis for HICRs in the GM12878 cell line. The top 10 terms are displayed, ordered by the negative log10, which is displayed on the x-axis. In GM12878, a B-lymphocytes cell line, terms related to immune response were highly enriched. **c**, Spatial pattern of the histone marks found in a window of 100 kb adjacent to the HICRs. The signal was averaged over all samples. The average signal over non-HICRs is illustrated in a lighter colour. In general, histone marks that are linked to transcriptional activity (acetylations, H3K36me3, H3K4me1) had an increased signal.

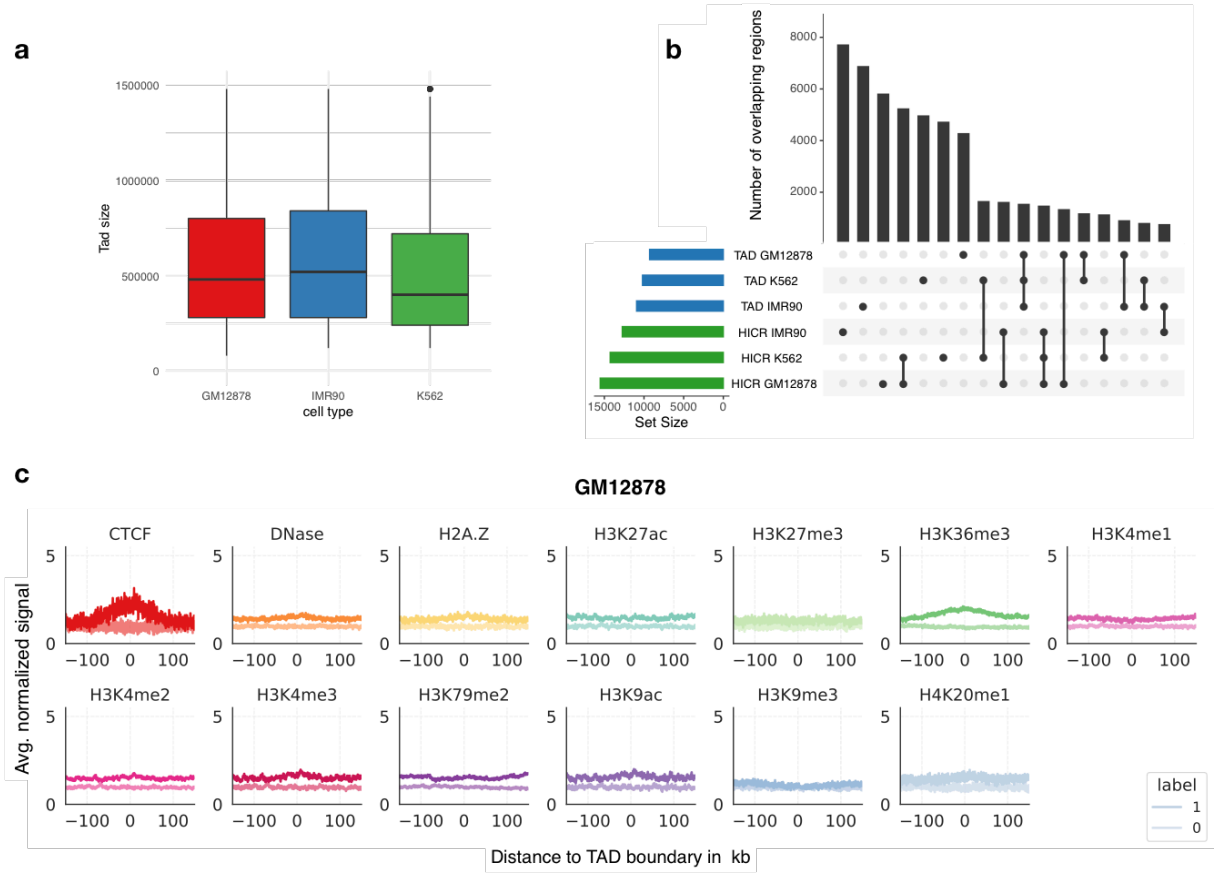

Fig. 3. Inspection of TAD boundaries. **a**, Distribution of the sizes of identified TADs for all three cell-types. Most TADs had sizes between 0.2 Mb and 0.75 Mb with a mean of 0.5 Mb. This was in accordance with previous studies. **b**, Overlap of identified HICRs and TAD boundaries in all three cell-types and overlap of HICRs and TAD boundaries in the same cell type. HICRs showed little overlap,**c**, Spatial pattern of the histone marks found in a window of 300 kb adjacent to the TAD boundaries. The signal was averaged over all samples. The average signal over non-TAD boundaries is illustrated in a lighter colour. Compared to the HICRs, the signal was a lot weaker and the peaks broader. Most importantly, CTCF and H3K36me3 – both well-known markers of TAD boundaries – were enriched.

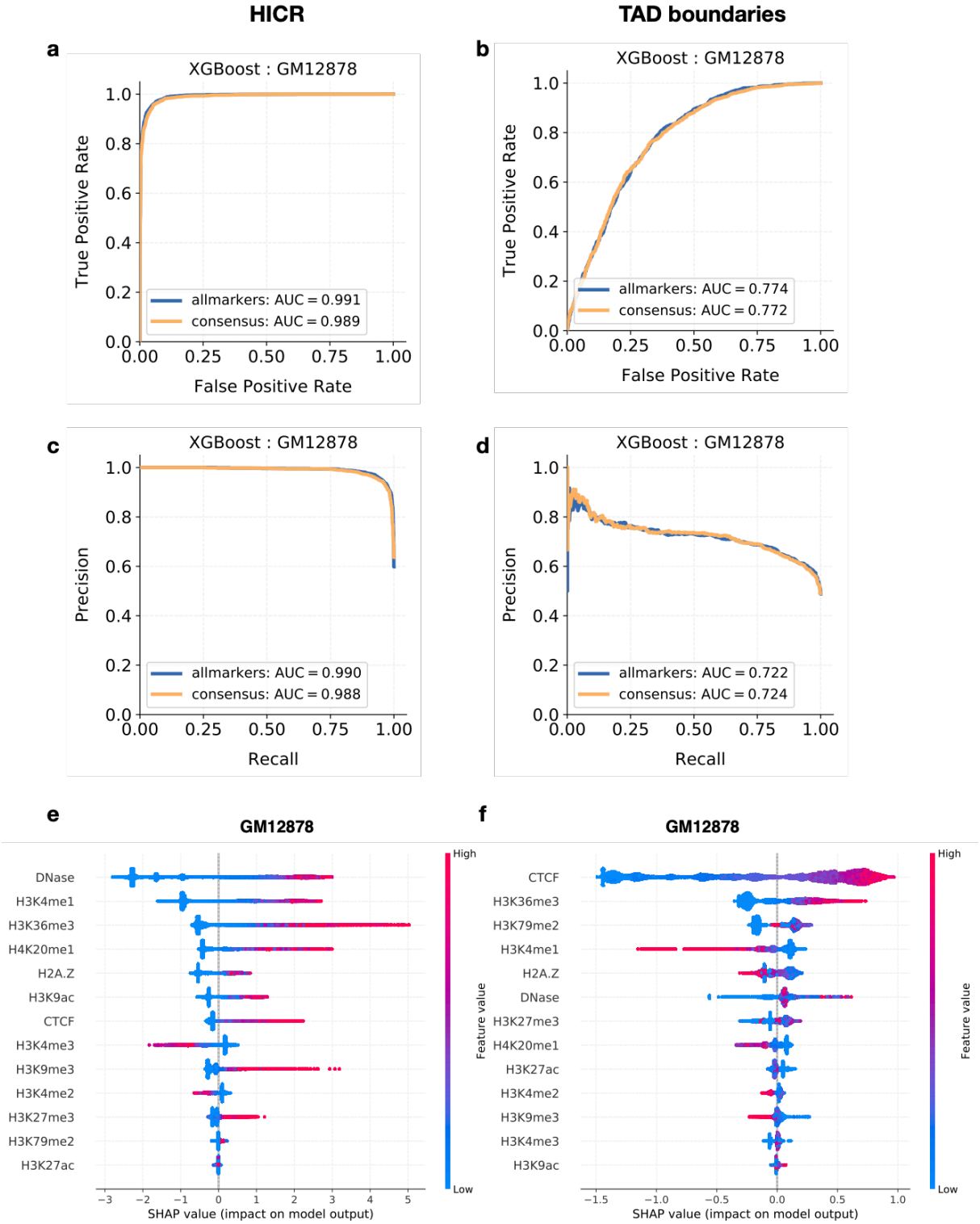

Fig. 4. XGBoost performance and Feature importance on GM12878. a-b Receiver-operating characteristic curve and **c-d** precision-recall curve for the binary classification task of predicting HICRs (**a**, **c**) and TAD boundaries (**b**, **d**) from histone mark data. Models were trained once using all available histone marks for each cell type (blue) and using only the consensus set (orange). **e-f** Histone marks ordered by mean absolute SHAP values in HICRs (**e**) and TAD boundaries (**f**). On the y axis, the violin plot shows the full distribution of the SHAP values for each feature. The dot plot in the foreground shows a color coding of the actual value of the feature, resulting in the SHAP value as indicated on the x axis.

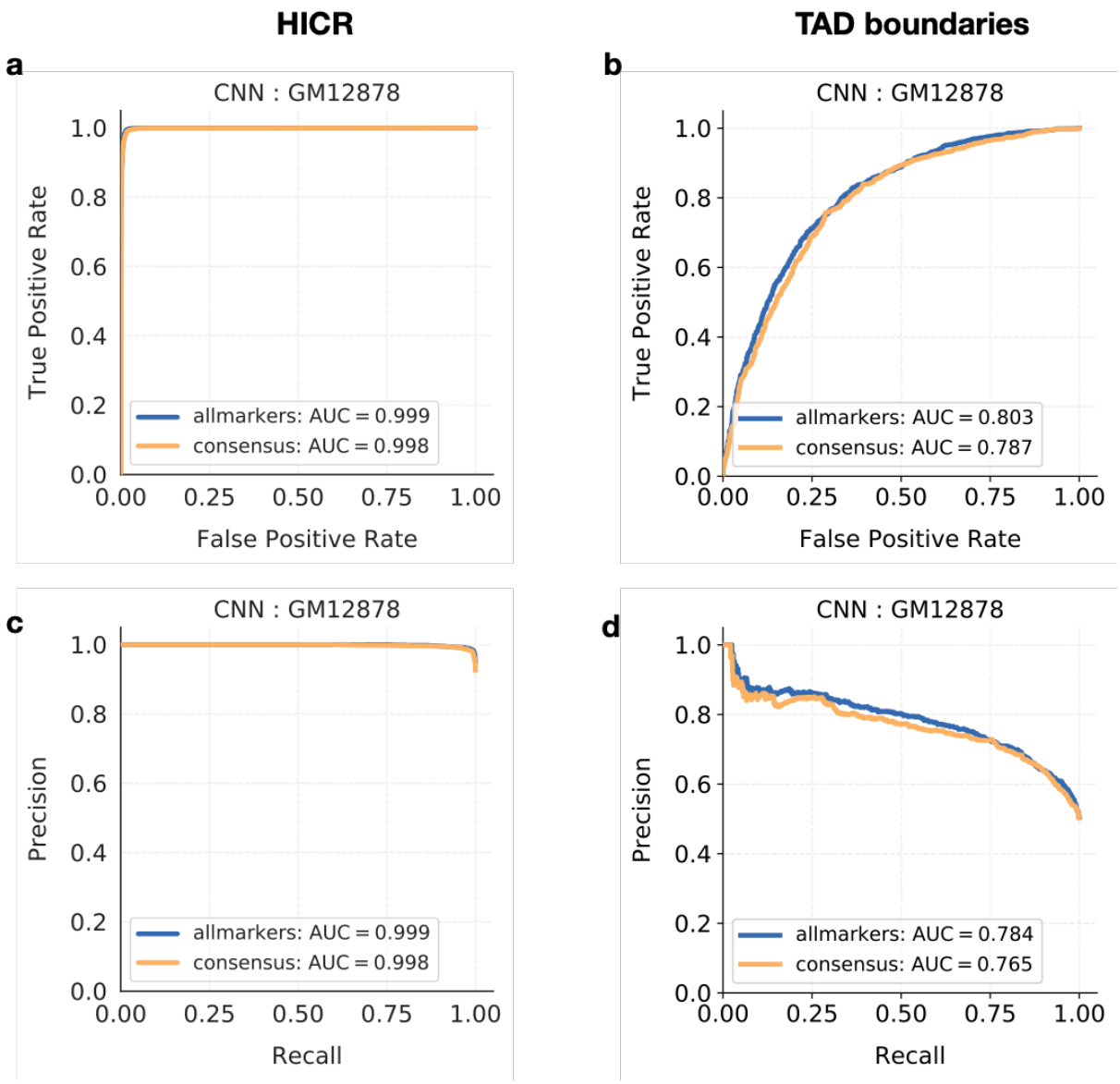

Fig. 5. CNN performance on GM12878. a-b Receiver-operating characteristic curve and **c-d** precision-recall curve for the binary classification task of predicting HICRs (**a**, **c**) and TAD boundaries (**b**, **d**) from histone mark data. Models were trained once using all available histone marks for each cell type (blue) and using only the consensus set (orange). CNNs outperformed the XGBoost model.

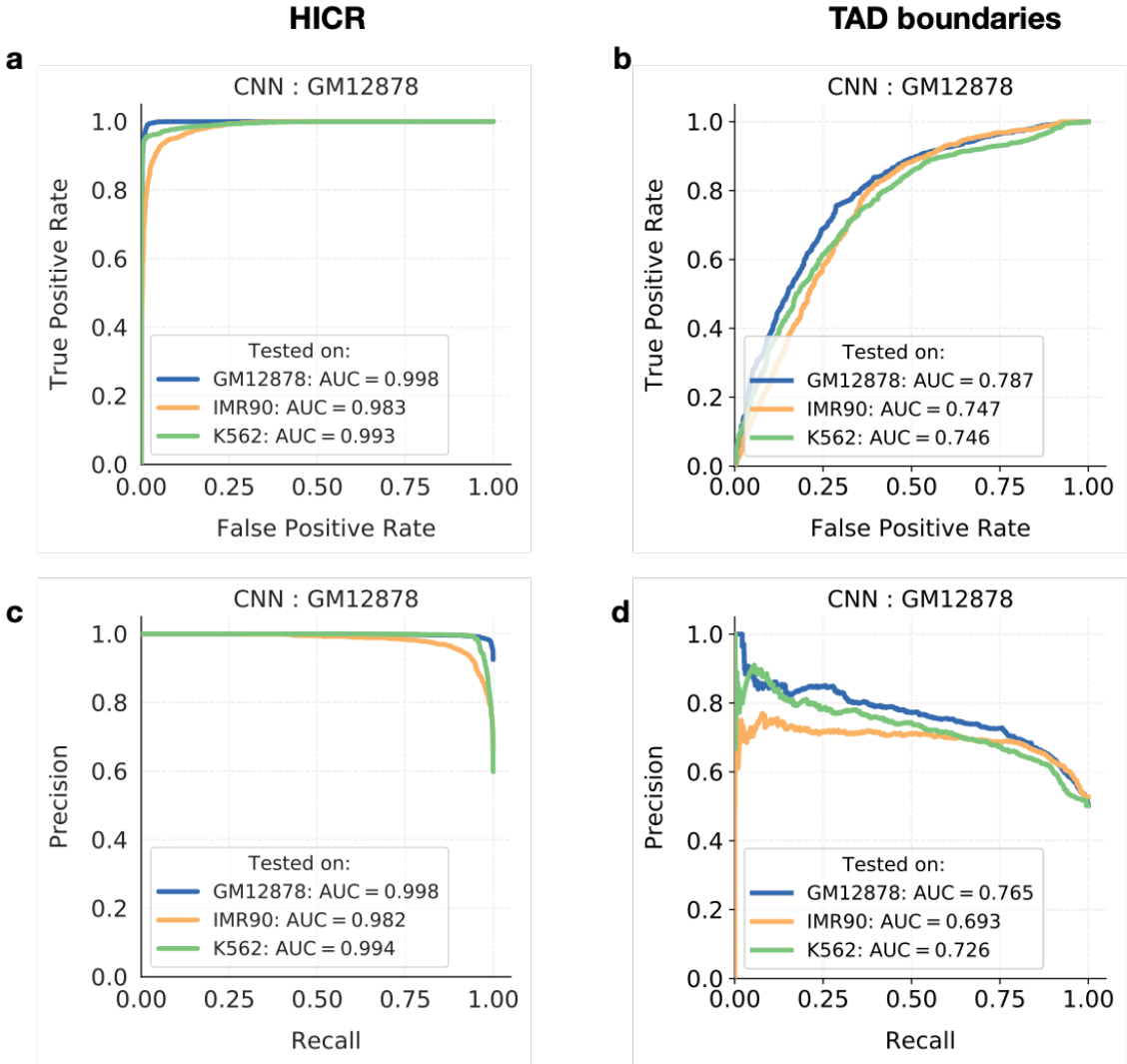

Fig. 6. Cross-cell performance on GM12878. a-b Receiver-operating characteristic curve and **c-d** precision-recall curve for the binary classification task of predicting HICRs (**a**, **c**) and TAD boundaries (**b**, **d**) in all three cell types from models solely trained on GM12878 data. Models were trained using only the consensus set.

References

1. T. Cremer and C. Cremer, "Chromosome territories, nuclear architecture and gene regulation in mammalian cells," *Nature Reviews Genetics*, vol. 2, no. 4, pp. 292–301, 2001.

2. T. Sexton, H. Schober, P. Fraser, and S. M. Gasser, "Gene regulation through nuclear organization," *Nature Structural and Molecular Biology*, vol. 14, no. 11, pp. 1049–1055, 2007.

3. W. A. Bickmore, "The Spatial Organization of the Human Genome," *Annual Review of Genomics and Human Genetics*, vol. 14, no. 1, pp. 67–84, 2013.

4. K. Luger, A. W. Mäder, R. K. Richmond, D. F. Sargent, and T. J. Richmond, "Crystal structure of the nucleosome core particle at 2.8 å resolution," *Nature*, vol. 389, no. 6648, pp. 251–260, 1997.

5. V. Allfrey, R. Faulkner, and A. Mirsky, "Acetylation and methylation of histones and their possible role in the regulation of rna synthesis," *Proceedings of the National Academy of Sciences*, vol. 51, no. 5, pp. 786–794, 1964.

6. A. J. Ruthenburg, H. Li, D. J. Patel, and C. D. Allis, "Multivalent engagement of chromatin modifications by linked binding modules," *Nature reviews Molecular cell biology*, vol. 8, no. 12, pp. 983–994, 2007.

7. C. D. Allis, L. M. Caparros, T. Jenuwein, and D. Reinberg, *Epigenetics*. Cold Spring Harbor, NY: Cold Spring Harbor Laboratory Press, 2nd ed., 2015.

8. J. R. Ecker, W. A. Bickmore, I. Barroso, J. K. Pritchard, Y. Gilad, and E. Segal, "ENCODE explained," *Nature*, vol. 489, p. 52, sep 2012.

9. T. J. Stevens, D. Lando, S. Basu, L. P. Atkinson, Y. Cao, S. F. Lee, M. Leeb, K. J. Wohlfahrt, W. Boucher, A. O'Shaughnessy-Kirwan, *et al.*, "3d structures of individual mammalian genomes studied by single-cell hi-c," *Nature*, vol. 544, no. 7648, pp. 59–64, 2017.

10. G. Li, X. Ruan, R. Auerbach, K. Sandhu, M. Zheng, P. Wang, H. Poh, Y. Goh, J. Lim, J. Zhang, H. Sim, S. Peh, F. Mulawadi, C. Ong, Y. Orlov, S. Hong, Z. Zhang, S. Landt, D. Raha, G. Euskirchen, C.-L. Wei, W. Ge, H. Wang, C. Davis, K. I. Fisher-Aylor, A. Mortazavi, M. Gerstein, T. Gingeras, B. Wold, Y. Sun, M. Fullwood, E. Cheung, E. Liu, W.-K. Sung, M. Snyder, and Y. Ruan, "Extensive Promoter-Centered Chromatin Interactions Provide a Topological Basis for Transcription Regulation," *Cell*, vol. 148, pp. 84–98, jan 2012.

11. A. Sanyal, B. R. Lajoie, G. Jain, and J. Dekker, "The long-range interaction landscape of gene promoters," *Nature*, vol. 489, pp. 109–113, sep 2012.

12. F. Jin, Y. Li, J. R. Dixon, S. Selvaraj, Z. Ye, A. Y. Lee, C. A. Yen, A. D. Schmitt, C. A. Espinoza, and B. Ren, "A high-resolution map of the three-dimensional chromatin interactome in human cells," *Nature*, vol. 503, no. 7475, pp. 290–294, 2013.

13. J. Dowen, Z. Fan, D. Hnisz, G. Ren, B. Abraham, L. Zhang, A. Weintraub, J. Schuijers, T. Lee, K. Zhao, and R. Young, "Control of Cell Identity Genes Occurs in Insulated Neighborhoods in Mammalian Chromosomes," *Cell*, vol. 159, pp. 374–387, oct 2014.

14. N. Heidari, D. H. Phanstiel, C. He, F. Grubert, F. Jahanbani, M. Kasowski, M. Q. Zhang, and M. P. Snyder, "Genome-wide map of regulatory interactions in the human genome.," *Genome research*, vol. 24, pp. 1905–17, dec 2014.

15. M. Simonis, P. Klous, E. Splinter, Y. Moshkin, R. Willemsen, E. De Wit, B. Van Steensel, and W. De Laat, "Nuclear organization of active and inactive chromatin domains uncovered by chromosome conformation capture–on-chip (4c)," *Nature genetics*, vol. 38, no. 11, pp. 1348–1354, 2006.

16. J. Dostie, T. A. Richmond, R. A. Arnaout, R. R. Selzer, W. L. Lee, T. A. Honan, E. D. Rubio, A. Krumm, J. Lamb, C. Nusbaum, *et al.*, "Chromosome conformation capture carbon copy (5c): a massively parallel solution for mapping interactions between genomic elements," *Genome research*, vol. 16, no. 10, pp. 1299–1309, 2006.

17. E. Lieberman-Aiden, N. L. Van Berkum, L. Williams, M. Imakaev, T. Ragoczy, A. Telling, I. Amit, B. R. Lajoie, P. J. Sabo, M. O. Dorschner, *et al.*, "Comprehensive mapping of long-range interactions reveals folding principles of the human genome," *science*, vol. 326, no. 5950, pp. 289–293, 2009.

18. M. J. Fullwood, M. H. Liu, Y. F. Pan, J. Liu, H. Xu, Y. B. Mohamed, Y. L. Orlov, S. Velkov, A. Ho, P. H. Mei, *et al.*, "An oestrogen-receptor-α-bound human chromatin interactome," *Nature*, vol. 462, no. 7269, pp. 58–64, 2009.

19. A. D. Schmitt, M. Hu, and B. Ren, "Genome-wide mapping and analysis of chromosome architecture," *Nature Reviews Molecular Cell Biology*, vol. 17, no. 12, pp. 743–755, 2016.

20. E. Lieberman-Aiden, N. L. V. Berkum, L. Williams, M. Imakaev, T. Ragoczy, A. Telling, I. Amit, B. R. Lajoie, P. J. Sabo, M. O. Dorschner, R. Sandstrom, B. Bernstein, M. A. Bender, M. Groudine, A. Gnirke, J. Stamatoyannopoulos, and L. A. Mirny, "Comprehensive Mapping of Long-Range Interactions Reveals Folding Principles of the Human Genome," *Science*, vol. 33292, no. October, pp. 289–294, 2009.

21. J. R. Dixon, D. U. Gorkin, and B. Ren, "Chromatin Domains: The Unit of Chromosome Organization," *Molecular Cell*, vol. 62, no. 5, pp. 668–680, 2016.

22. E. P. Nora, B. R. Lajoie, E. G. Schulz, L. Giorgetti, I. Okamoto, N. Servant, T. Piolot, N. L. Van Berkum, J. Meisig, J. Sedat, J. Gribnau, E. Barillot, N. Blüthgen, J. Dekker, and E. Heard, "Spatial partitioning of the regulatory landscape of the X-inactivation centre," *Nature*, vol. 485, no. 7398, pp. 381–385, 2012.

23. S. S. Rao, M. H. Huntley, N. C. Durand, E. K. Stamenova, I. D. Bochkov, J. T. Robinson, A. L. Sanborn, I. Machol, A. D. Omer, E. S. Lander, and E. L. Aiden, "A 3D map of the human genome at kilobase resolution reveals principles of chromatin looping," *Cell*, vol. 159, no. 7, pp. 1665–1680, 2014.

24. J. R. Dixon, S. Selvaraj, F. Yue, A. Kim, Y. Li, Y. Shen, M. Hu, J. S. Liu, and B. Ren, "Topological domains in mammalian genomes identified by analysis of chromatin interactions," *Nature*, vol. 485, no. 7398, pp. 376–380, 2012.

25. B. M. Javierre, O. S. Burren, S. P. Wilder, R. Kreuzhuber, S. M. Hill, S. Sewitz, J. Cairns, S. W. Wingett, C. Várnai, M. J. Thiecke, *et al.*, "Lineage-specific genome architecture links enhancers and non-coding disease variants to target gene promoters," *Cell*, vol. 167, no. 5, pp. 1369–1384, 2016.

26. E. Rodríguez-Carballo, L. Lopez-Delisle, Y. Zhan, P. J. Fabre, L. Beccari, I. El-Idrissi, T. H. N. Huynh, H. Ozadam, J. Dekker, and D. Duboule, "The hoxd cluster is a dynamic and resilient tad boundary controlling the segregation of antagonistic regulatory landscapes," *Genes & development*, vol. 31, no. 22, pp. 2264–2281, 2017.

27. O. Symmons, V. V. Uslu, T. Tsujimura, S. Ruf, S. Nassari, W. Schwarzer, L. Ettwiller, and F. Spitz, "Functional and topological characteristics of mammalian regulatory domains," *Genome research*, vol. 24, no. 3, pp. 390–400, 2014.

28. Y. Shen, F. Yue, D. F. McCleary, Z. Ye, L. Edsall, S. Kuan, U. Wagner, J. Dixon, L. Lee, V. V. Lobanenkov, *et al.*, "A map of the cis-regulatory sequences in the mouse genome," *Nature*, vol. 488, no. 7409, pp. 116–120, 2012.

29. W. A. Flavahan, Y. Drier, B. B. Liau, S. M. Gillespie, A. S. Venteicher, A. O. Stemmer-Rachamimov, M. L. Suvà, and B. E. Bernstein, "Insulator dysfunction and oncogene activation in idh mutant gliomas," *Nature*, vol. 529, no. 7584, pp. 110–114, 2016.

30. J. R. Dixon, I. Jung, S. Selvaraj, Y. Shen, J. E. Antosiewicz-Bourget, A. Y. Lee, Z. Ye, A. Kim, N. Rajagopal, W. Xie, Y. Diao, J. Liang, H. Zhao, V. V. Lobanenkov, J. R. Ecker, J. A. Thomson, and B. Ren, "Chromatin architecture reorganization during stem cell differentiation," *Nature*, vol. 518, pp. 331–336, feb 2015.

31. J. Zuin, J. R. Dixon, M. I. J. A. van der Reijden, Z. Ye, P. Kolovos, R. W. W. Brouwer, M. P. C. van de Corput, H. J. G. van de Werken, T. A. Knoch, W. F. J. van IJcken, F. G. Grosveld, B. Ren, and K. S. Wendt, "Cohesin and CTCF differentially affect chromatin architecture and gene expression in human cells.," *Proceedings of the National Academy of Sciences of the United States of America*, vol. 111, pp. 996–1001, jan 2014.

32. M. Vietri Rudan, C. Barrington, S. Henderson, C. Ernst, D. Odom, A. Tanay, and S. Hadjur, "Comparative Hi-C Reveals that CTCF Underlies Evolution of Chromosomal Domain Architecture," *Cell Reports*, vol. 10, pp. 1297–1309, mar 2015.

33. G. Fudenberg, M. Imakaev, C. Lu, A. Goloborodko, N. Abdennur, and L. A. Mirny, "Formation of Chromosomal Domains by Loop Extrusion," *Cell Reports*, vol. 15, pp. 2038–2049, may 2016.

34. A. L. Sanborn, S. S. P. Rao, S.-C. Huang, N. C. Durand, M. H. Huntley, A. I. Jewett, I. D. Bochkov, D. Chinnappan, A. Cutkosky, J. Li, K. P. Geeting, A. Gnirke, A. Melnikov, D. McKenna, E. K. Stamenova, E. S. Lander, and E. L. Aiden, "Chromatin extrusion explains key features of loop and domain formation in wild-type and engineered genomes," *Proceedings of the National Academy of Sciences*, vol. 112, pp. E6456–E6465, nov 2015.

35. M. J. Rowley and V. G. Corces, "Organizational principles of 3D genome architecture," *Nature Reviews Genetics*, vol. 19, no. 12, pp. 789–800, 2018.

36. Y. Guo, Q. Xu, D. Canzio, J. Shou, J. Li, D. Gorkin, I. Jung, H. Wu, Y. Zhai, Y. Tang, Y. Lu, Y. Wu, Z. Jia, W. Li, M. Zhang, B. Ren, A. Krainer, T. Maniatis, and Q. Wu, "CRISPR Inversion of CTCF Sites Alters Genome Topology and Enhancer/Promoter Function," *Cell*, vol. 162, pp. 900–910, aug 2015.

37. W. Schwarzer, N. Abdennur, A. Goloborodko, A. Pekowska, G. Fudenberg, Y. Loe-Mie, N. A. Fonseca, W. Huber, C. H. Haering, L. Mirny, and F. Spitz, "Two independent modes of chromatin organization revealed by cohesin removal," *Nature*, vol. 551, pp. 51–56, nov 2017.

38. S. S. P. Rao, S.-C. Huang, B. Glenn St Hilaire, J. M. Engreitz, E. M. Perez, K.-R. Kieffer-Kwon, A. L. Sanborn, S. E. Johnstone, G. D. Bascom, I. D. Bochkov, X. Huang, M. S. Shamim, J. Shin, D. Turner, Z. Ye, A. D. Omer, J. T. Robinson, T. Schlick, B. E. Bernstein, R. Casellas, E. S. Lander, and E. L. Aiden, "Cohesin Loss Eliminates All Loop Domains.," *Cell*, vol. 171, pp. 305–320.e24, oct 2017.

39. G. Fudenberg, N. Abdennur, M. Imakaev, A. Goloborodko, and L. A. Mirny, "Emerging Evidence of Chromosome Folding by Loop Extrusion," *Cold Spring Harbor Symposia on Quantitative Biology*, vol. 82, pp. 45–55, 2017.

40. Y. LeCun, Y. Bengio, and G. Hinton, "Deep learning," *nature*, vol. 521, no. 7553, pp. 436–444, 2015.

41. B. Alipanahi, A. Delong, M. T. Weirauch, and B. J. Frey, "Predicting the sequence specificities of dna-and rna-binding proteins by deep learning," *Nature biotechnology*, vol. 33, no. 8, pp. 831–838, 2015.

42. E. Moen, D. Bannon, T. Kudo, W. Graf, M. Covert, and D. Van Valen, "Deep learning for cellular image analysis," *Nature methods*, pp. 1–14, 2019.

43. A. W. Senior, R. Evans, J. Jumper, J. Kirkpatrick, L. Sifre, T. Green, C. Qin, A. Žídek, A. W. Nelson, A. Bridgland, *et al.*, "Improved protein structure prediction using potentials from deep learning," *Nature*, pp. 1–5, 2020.

44. A. Esteva, B. Kuprel, R. A. Novoa, J. Ko, S. M. Swetter, H. M. Blau, and S. Thrun, "Dermatologist-level classification of skin cancer with deep neural networks," *Nature*, vol. 542, no. 7639, pp. 115–118, 2017.

45. V. Gulshan, L. Peng, M. Coram, M. C. Stumpe, D. Wu, A. Narayanaswamy, S. Venugopalan, K. Widner, T. Madams, J. Cuadros, *et al.*, "Development and validation of a deep learning algorithm for detection of diabetic retinopathy in retinal fundus photographs," *Jama*, vol. 316, no. 22, pp. 2402–2410, 2016.

46. M. Komorowski, L. A. Celi, O. Badawi, A. C. Gordon, and A. A. Faisal, "The artificial intelligence clinician learns optimal treatment strategies for sepsis in intensive care," *Nature medicine*, vol. 24, no. 11, pp. 1716–1720, 2018.

47. R. EpigenomicsConsortium, "Integrative analysis of 111 reference human epigenomes," *Nature*, vol. 518, p. 317, feb 2015.

48. H. Li and R. Durbin, "Fast and accurate short read alignment with burrows–wheeler transform," *bioinformatics*, vol. 25, no. 14, pp. 1754–1760, 2009.

49. M. Martin, "Cutadapt removes adapter sequences from high-throughput sequencing reads," *EMBnet. journal*, vol. 17, no. 1, pp. 10–12, 2011.

50. E. P. Consortium *et al.*, "An integrated encyclopedia of dna elements in the human genome," *Nature*, vol. 489, no. 7414, pp. 57–74, 2012.

51. T. S. Carroll, Z. Liang, R. Salama, R. Stark, and I. de Santiago, "Impact of artifact removal on chip quality metrics in chip-seq and chip-exo data," *Frontiers in genetics*, vol. 5, p. 75, 2014.

52. Y. Zhang, T. Liu, C. A. Meyer, J. Eeckhoute, D. S. Johnson, B. E. Bernstein, C. Nusbaum, R. M. Myers, M. Brown, W. Li, *et al.*, "Model-based analysis of chip-seq (macs)," *Genome biology*, vol. 9, no. 9, p. R137, 2008.

53. B. Alberts, *Molecular Biology of the Cell.* Garland Science, 6th. ed., 2017.

54. C. M. Bishop and C. M., *Neural networks for pattern recognition.* Clarendon Press, 1995.

55. N. Servant, N. Varoquaux, B. R. Lajoie, E. Viara, C.-J. Chen, J.-P. Vert, E. Heard, J. Dekker, and E. Barillot, "HiC-Pro: an optimized and flexible pipeline for Hi-C data processing," *Genome Biology*, vol. 16, no. 1, p. 259, 2015.

56. B. Langmead and S. L. Salzberg, "Fast gapped-read alignment with bowtie 2," *Nature methods*, vol. 9, no. 4, p. 357, 2012.

57. M. Imakaev, G. Fudenberg, R. P. McCord, N. Naumova, A. Goloborodko, B. R. Lajoie, J. Dekker, and L. A. Mirny, "Iterative correction of Hi-C data reveals hallmarks of chromosome organization," *Nature Methods*, vol. 9, no. 10, pp. 999–1003, 2012.

58. F. Ay, T. L. Bailey, and W. S. Noble, "Statistical confidence estimation for Hi-C data reveals regulatory chromatin contacts," *Genome Research*, vol. 24, no. 6, pp. 999–1011, 2014.

59. F. Serra, D. Baù, M. Goodstadt, D. Castillo, G. Filion, and M. A. Marti-Renom, "Automatic analysis and 3D-modelling of Hi-C data using TADbit reveals structural features of the fly chromatin colors," *PLoS Computational Biology*, vol. 13, no. 7, pp. 1–17, 2017.

60. F. L. Dily, D. Baù, A. Pohl, G. P. Vicent, F. Serra, D. Soronellas, G. Castellano, R. H. Wright, C. Ballare, G. Filion, M. A. Marti-Renom, and M. Beato, "Distinct structural transitions of chromatin topological domains correlate with coordinated hormone-induced gene regulation," *Genes & Development*, vol. 28, pp. 2151–2162, oct 2014.

61. C. Y. McLean, D. Bristor, M. Hiller, S. L. Clarke, B. T. Schaar, C. B. Lowe, A. M. Wenger, and G. Bejerano, "GREAT improves functional interpretation of cis-regulatory regions," *Nature Biotechnology*, vol. 28, pp. 495–501, may 2010.

62. Z. Gu, R. Eils, and M. Schlesner, "Complex heatmaps reveal patterns and correlations in multidimensional genomic data," *Bioinformatics*, vol. 32, pp. 2847–2849, 05 2016.

63. A. R. Quinlan and I. M. Hall, "Bedtools: a flexible suite of utilities for comparing genomic features," *Bioinformatics*, vol. 26, no. 6, pp. 841–842, 2010.

64. J. Bergstra, D. Yamins, and D. D. Cox, "Making a science of model search: Hyperparameter optimization in hundreds of dimensions for vision architectures," *Jmlr*, 2013.

65. T. Chen and C. Guestrin, "Xgboost," *Proceedings of the 22nd ACM SIGKDD International Conference on Knowledge Discovery and Data Mining - KDD '16*, 2016.

66. F. Pedregosa, G. Varoquaux, A. Gramfort, V. Michel, B. Thirion, O. Grisel, M. Blondel, P. Prettenhofer, R. Weiss, V. Dubourg, J. Vanderplas, A. Passos, D. Cournapeau, M. Brucher, M. Perrot, and E. Duchesnay, "Scikit-learn: Machine learning in Python," *Journal of Machine Learning Research*, vol. 12, pp. 2825–2830, 2011.

67. D. P. Kingma and J. Ba, "Adam: A method for stochastic optimization," *arXiv preprint arXiv:1412.6980*, 2014.

68. Z. Xu, H. Wang, S. Wei, Z. Wang, and G. Ji, "Inhibition of er stress-related ire1α/creb/nlrp1 pathway promotes the apoptosis of human chronic myelogenous leukemia cell," *Molecular immunology*, vol. 101, pp. 377–385, 2018.

69. Z. Wang, C. Zang, J. A. Rosenfeld, D. E. Schones, A. Barski, S. Cuddapah, K. Cui, T.-Y. Roh, W. Peng, M. Q. Zhang, *et al.*, "Combinatorial patterns of histone acetylations and methylations in the human genome," *Nature genetics*, vol. 40, no. 7, p. 897, 2008.

70. P. H. L. Krijger and W. de Laat, "Regulation of disease-associated gene expression in the 3D genome," *Nature Reviews Molecular Cell Biology*, vol. 17, pp. 771–782, dec 2016.

71. R. Bargaje, M. P. Alam, A. Patowary, M. Sarkar, T. Ali, S. Gupta, M. Garg, M. Singh, R. Purkanti, V. Scaria, *et al.*, "Proximity of h2a. z containing nucleosome to the transcription start site influences gene expression levels in the mammalian liver and brain," *Nucleic acids research*, vol. 40, no. 18, pp. 8965–8978, 2012.

72. B. Bonev, N. M. Cohen, Q. Szabo, L. Fritsch, G. L. Papadopoulos, Y. Lubling, X. Xu, X. Lv, J.-P. Hugnot, A. Tanay, *et al.*, "Multiscale 3d genome rewiring during mouse neural development," *Cell*, vol. 171, no. 3, pp. 557–572, 2017.

73. M. J. Rowley, M. H. Nichols, X. Lyu, M. Ando-Kuri, I. S. M. Rivera, K. Hermetz, P. Wang, Y. Ruan, and V. G. Corces, "Evolutionarily conserved principles predict 3d chromatin organization," *Molecular cell*, vol. 67, no. 5, pp. 837–852, 2017.

74. D. G. Lupiáñez, K. Kraft, V. Heinrich, P. Krawitz, F. Brancati, E. Klopocki, D. Horn, H. Kayserili, J. M. Opitz, R. Laxova, *et al.*, "Disruptions of topological chromatin domains cause pathogenic rewiring of gene-enhancer interactions," *Cell*, vol. 161, no. 5, pp. 1012–1025, 2015.

75. A. Despang, R. Schöpflin, M. Franke, S. Ali, I. Jerković, C. Paliou, W.-L. Chan, B. Timmermann, L. Wittler, M. Vingron, *et al.*, "Functional dissection of the sox9-kcnj2 locus identifies nonessential and instructive roles of tad architecture," *Nature genetics*, vol. 51, no. 8, pp. 1263–1271, 2019.

76. E. P. Nora, A. Goloborodko, A.-L. Valton, J. H. Gibcus, A. Uebersohn, N. Abdennur, J. Dekker, L. A. Mirny, and B. G. Bruneau, "Targeted degradation of ctcf decouples local insulation of chromosome domains from genomic compartmentalization," *Cell*, vol. 169, no. 5, pp. 930–944, 2017.

77. B. D. Pope, T. Ryba, V. Dileep, F. Yue, W. Wu, O. Denas, D. L. Vera, Y. Wang, R. S. Hansen, T. K. Canfield, *et al.*, "Topologically associating domains are stable units of replication-timing regulation," *Nature*, vol. 515, no. 7527, pp. 402–405, 2014.

78. J. Henderson, V. Ly, S. Olichwier, P. Chainani, Y. Liu, and B. Soibam, "Accurate prediction of boundaries of high resolution topologically associated domains (tads) in fruit flies using deep learning," *Nucleic acids research*, vol. 47, no. 13, pp. e78–e78, 2019.

79. S. M. Lundberg and S.-I. Lee, "A unified approach to interpreting model predictions," in *Advances in neural information processing systems*, pp. 4765–4774, 2017.

80. J. Huang, E. Marco, L. Pinello, and G. C. Yuan, "Predicting chromatin organization using histone marks," *Genome Biology*, vol. 16, no. 1, pp. 1–11, 2015.

81. S. Schwartz, E. Meshorer, and G. Ast, "Chromatin organization marks exon-intron structure," *Nature structural & molecular biology*, vol. 16, no. 9, p. 990, 2009.

82. R. F. Luco, Q. Pan, K. Tominaga, B. J. Blencowe, O. M. Pereira-Smith, and T. Misteli, "Regulation of alternative splicing by histone modifications," *Science*, vol. 327, no. 5968, pp. 996–1000, 2010.

83. M. J. Carrozza, B. Li, L. Florens, T. Suganuma, S. K. Swanson, K. K. Lee, W.-J. Shia, S. Anderson, J. Yates, M. P. Washburn, *et al.*, "Histone h3 methylation by set2 directs deacetylation of coding regions by rpd3s to suppress spurious intragenic transcription," *Cell*, vol. 123, no. 4, pp. 581–592, 2005.

84. A. Rada-Iglesias, R. Bajpai, T. Swigut, S. A. Brugmann, R. A. Flynn, and J. Wysocka, "A unique chromatin signature uncovers early developmental enhancers in humans," *Nature*, vol. 470, no. 7333, pp. 279–283, 2011.

85. G. E. Zentner, P. J. Tesar, and P. C. Scacheri, "Epigenetic signatures distinguish multiple classes of enhancers with distinct cellular functions," *Genome research*, vol. 21, no. 8, pp. 1273–1283, 2011.

86. M. P. Creyghton, A. W. Cheng, G. G. Welstead, T. Kooistra, B. W. Carey, E. J. Steine, J. Hanna, M. A. Lodato, G. M. Frampton, P. A. Sharp, *et al.*, "Histone h3k27ac separates active from poised enhancers and predicts developmental state," *Proceedings of the National Academy of Sciences*, vol. 107, no. 50, pp. 21931–21936, 2010.

87. S. Heinz, C. E. Romanoski, C. Benner, and C. K. Glass, "The selection and function of cell type-specific enhancers," *Nature reviews Molecular cell biology*, vol. 16, no. 3, pp. 144–154, 2015.

88. W. Gan, J. Luo, Y. Z. Li, J. L. Guo, M. Zhu, and M. L. Li, "A computational method to predict topologically associating domain boundaries combining histone marks and sequence information," *BMC genomics*, vol. 20, no. 13, pp. 1–12, 2019.

89. S. Hong and D. Kim, "Computational characterization of chromatin domain boundary-associated genomic elements," *Nucleic acids research*, vol. 45, no. 18, pp. 10403–10414, 2017.

90. E. Sefer and C. Kingsford, "Semi-nonparametric modeling of topological domain formation from epigenetic data," *Algorithms for Molecular Biology*, vol. 14, no. 1, p. 4, 2019.

Supplementary Data

Figures

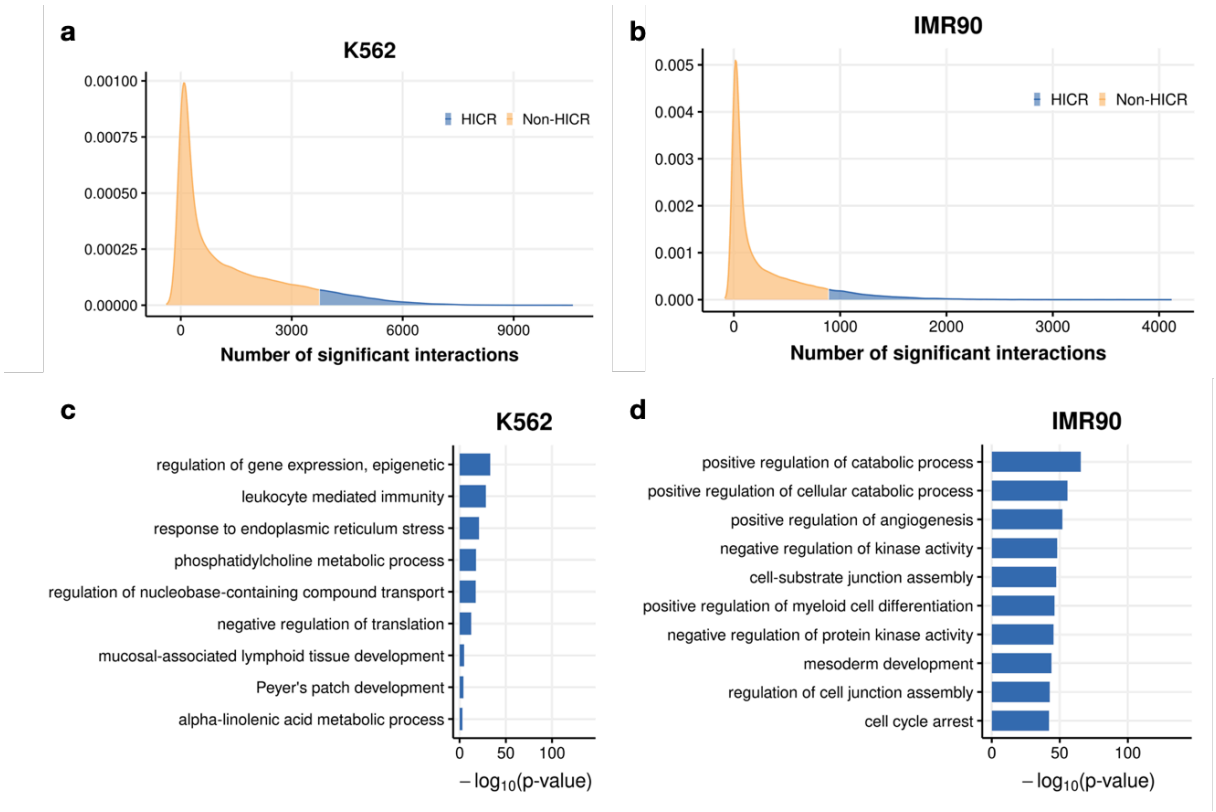

Fig. S1. Distribution of significant counts and GREAT analysis. a-b, The distribution of significant counts for the K562 (**a**) and IMR90 (**b**) cell line. Shaded in blue are the top 10% of all interactions, which were defined as Highly Interacting Chromatin Regions (HICRs). **c-d**, Functional enrichment analysis for HICRs in the K562 (**c**) and IMR90 (**d**) cell line. The top 10 terms are displayed, ordered by the negative log10, which is displayed on the x-axis.

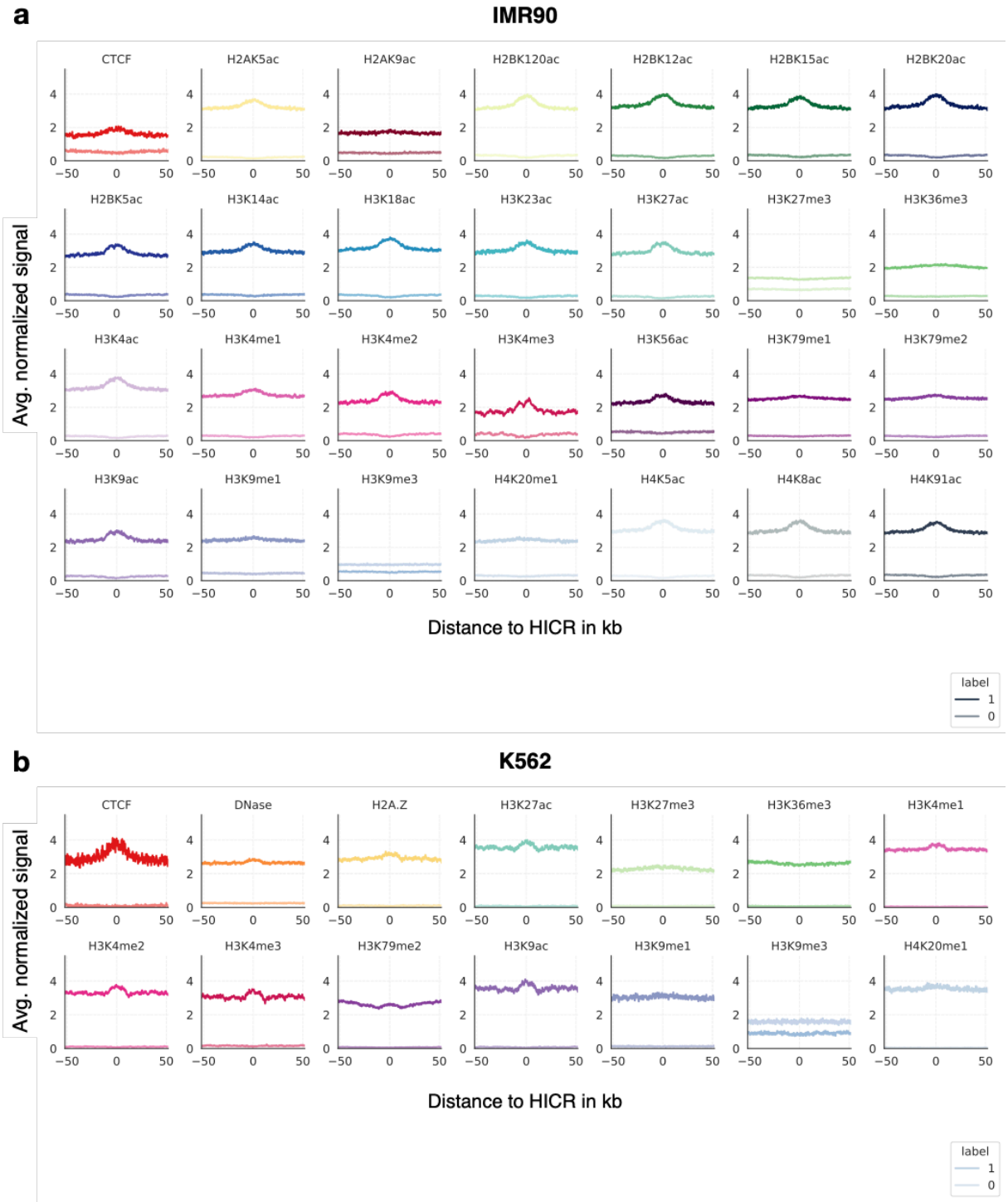

Fig. S2. Histone mark signal at HICRs. Spatial pattern of the histone marks found in a window of 100 kb adjacent to the HICRs for the IMR90 (**a**) and K562 (**b**) cell line. The signal was averaged over all samples. The average signal over non-HICRs is illustrated in a lighter colour.

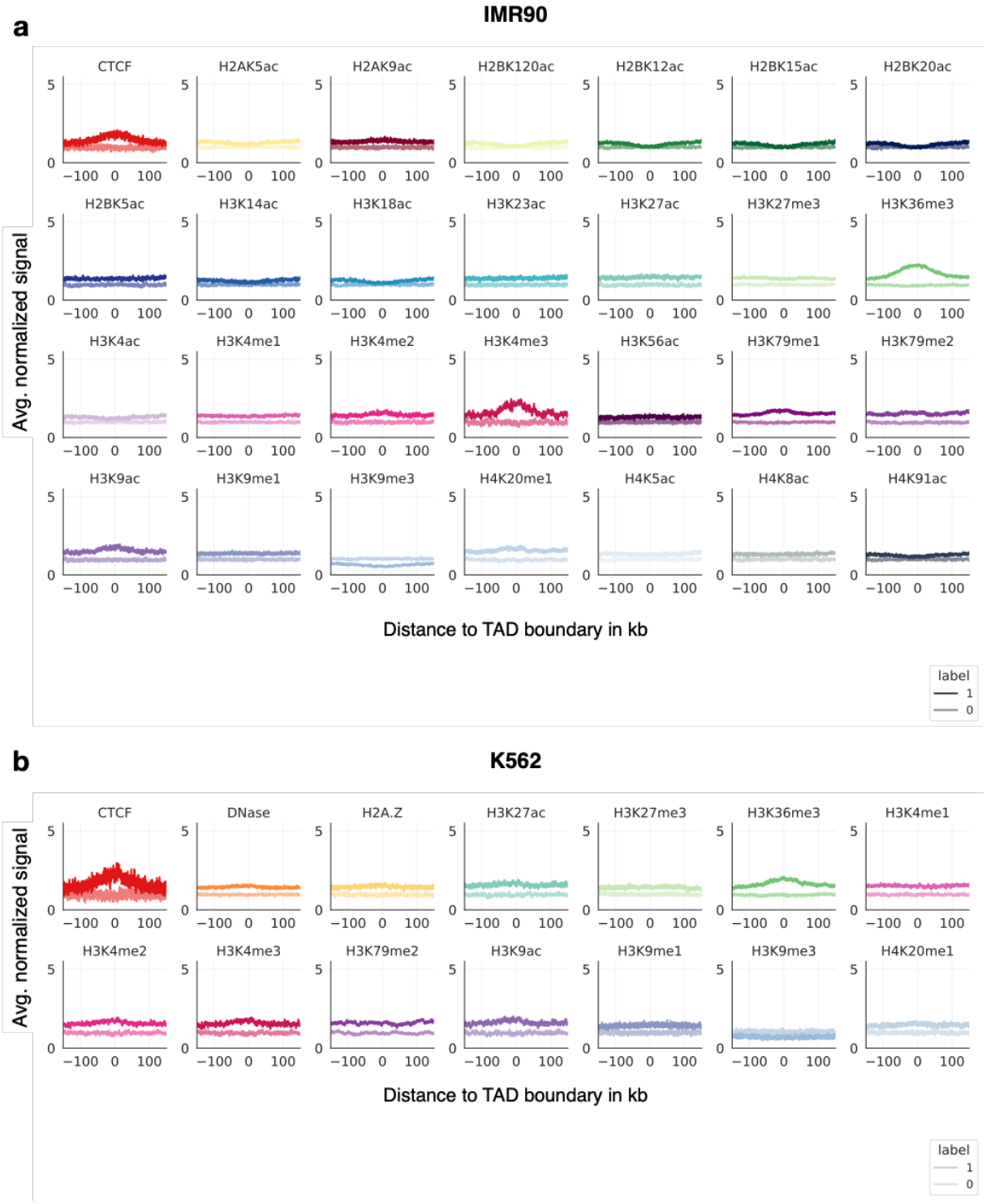

Fig. S3. Histone mark signal at TAD boundaries. Spatial pattern of the histone marks found in a window of 300 kb adjacent to the TAD boundaries for the IMR90 (**a**) and K562 (**b**) cell line. The signal was averaged over all samples. The average signal over non-TAD boundaries is illustrated in a lighter colour.

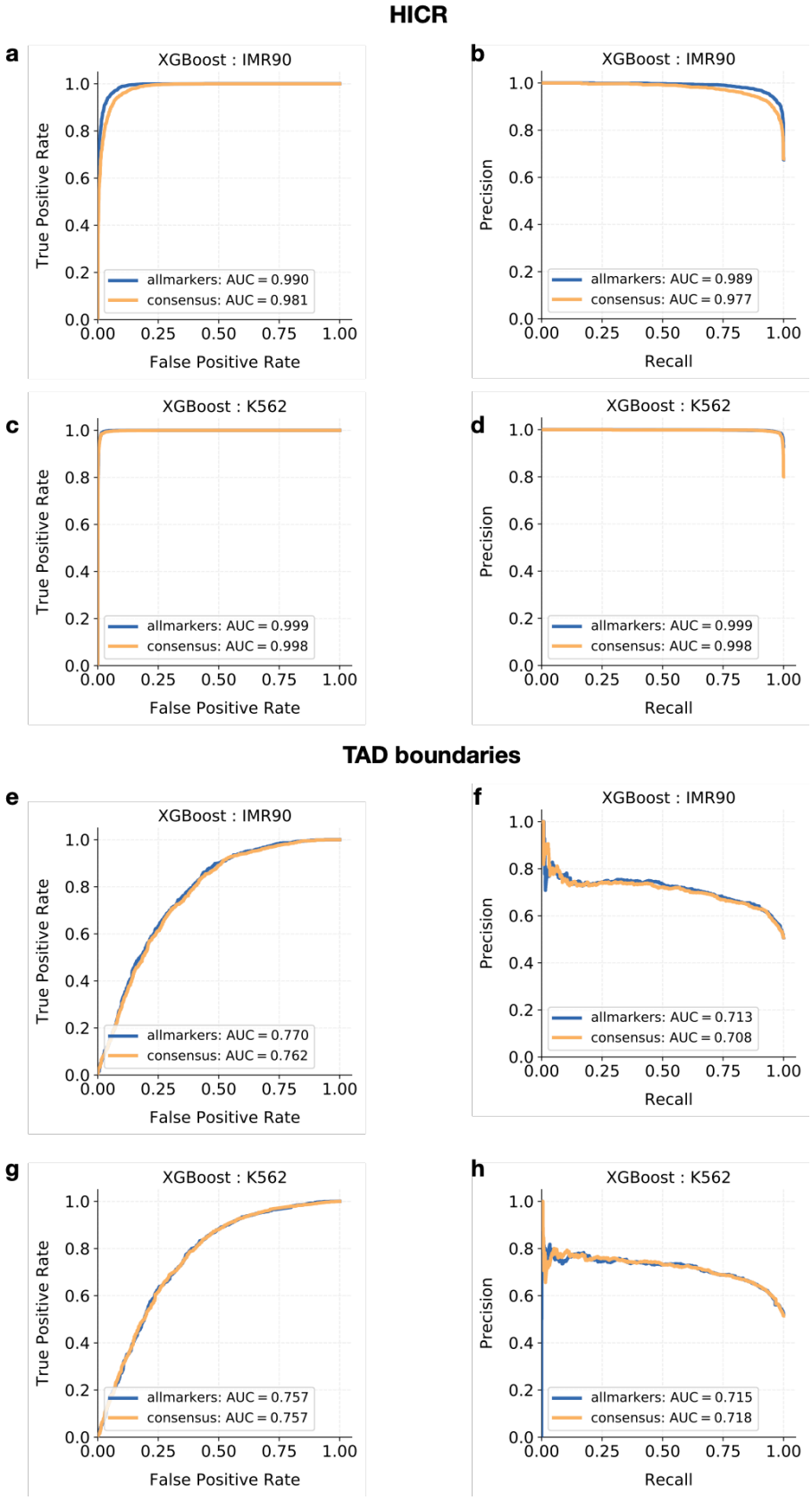

Fig. S4. XGBoost performance on IMR90 and K562. a,c,e,g Receiver-operating characteristic curve and **b,d,f,h** precision-recall curve for the binary classification task of predicting HICRs (**a-d**) and TAD boundaries (**e-h**) from histone mark data. Models were trained once using all available histone marks for each celltype (blue) and using only the consensus set (orange).

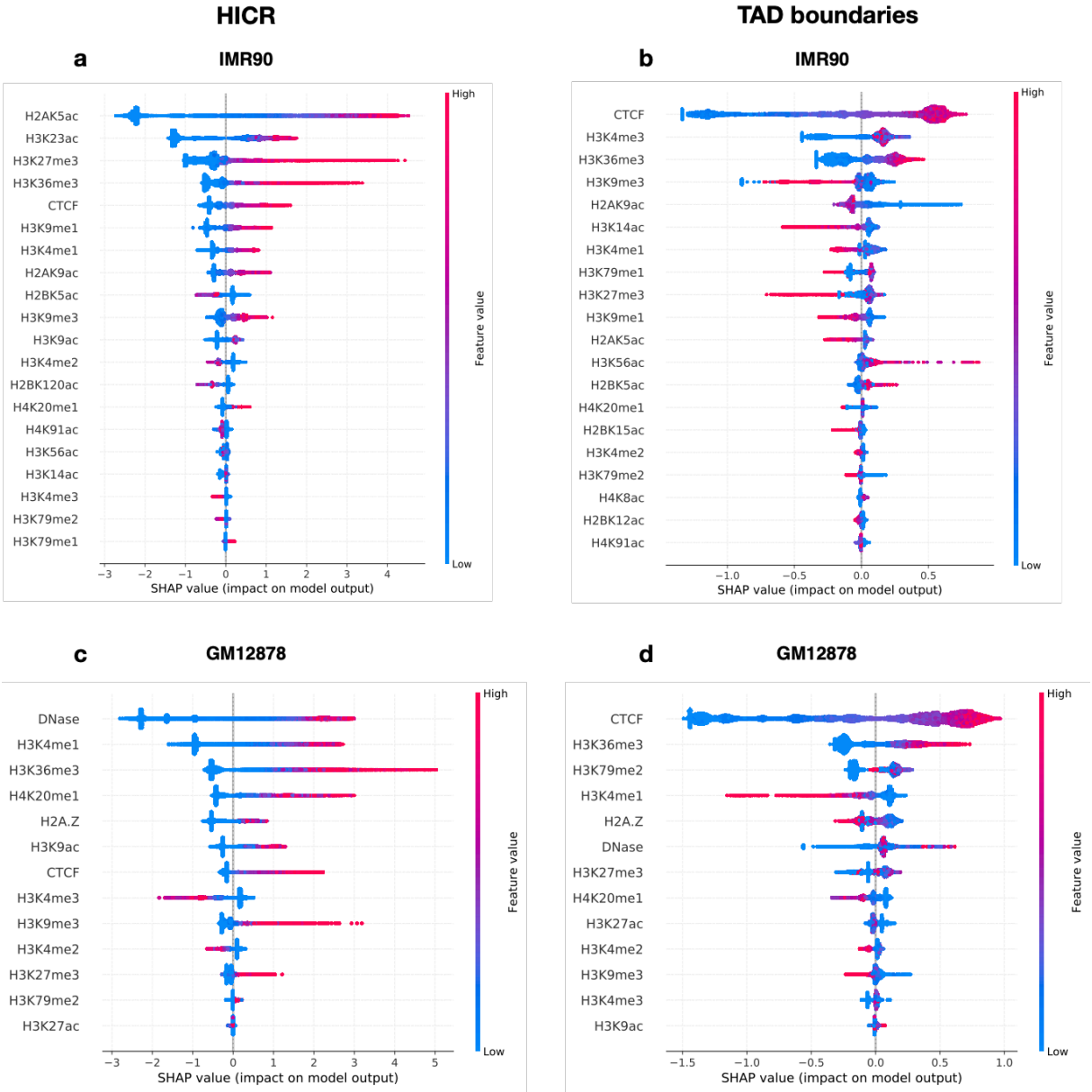

Fig. S5. Feature importance for IMR90 and K562. Histone marks ordered by mean absolute SHAP values in HICRs (**a,c**) and TAD boundaries (**b,d**). On the y axis, the violin plot shows the full distribution of the SHAP values for each feature. The dot plot in the foreground shows a color coding of the actual value of the feature, resulting in the SHAP value as indicated on the x axis.

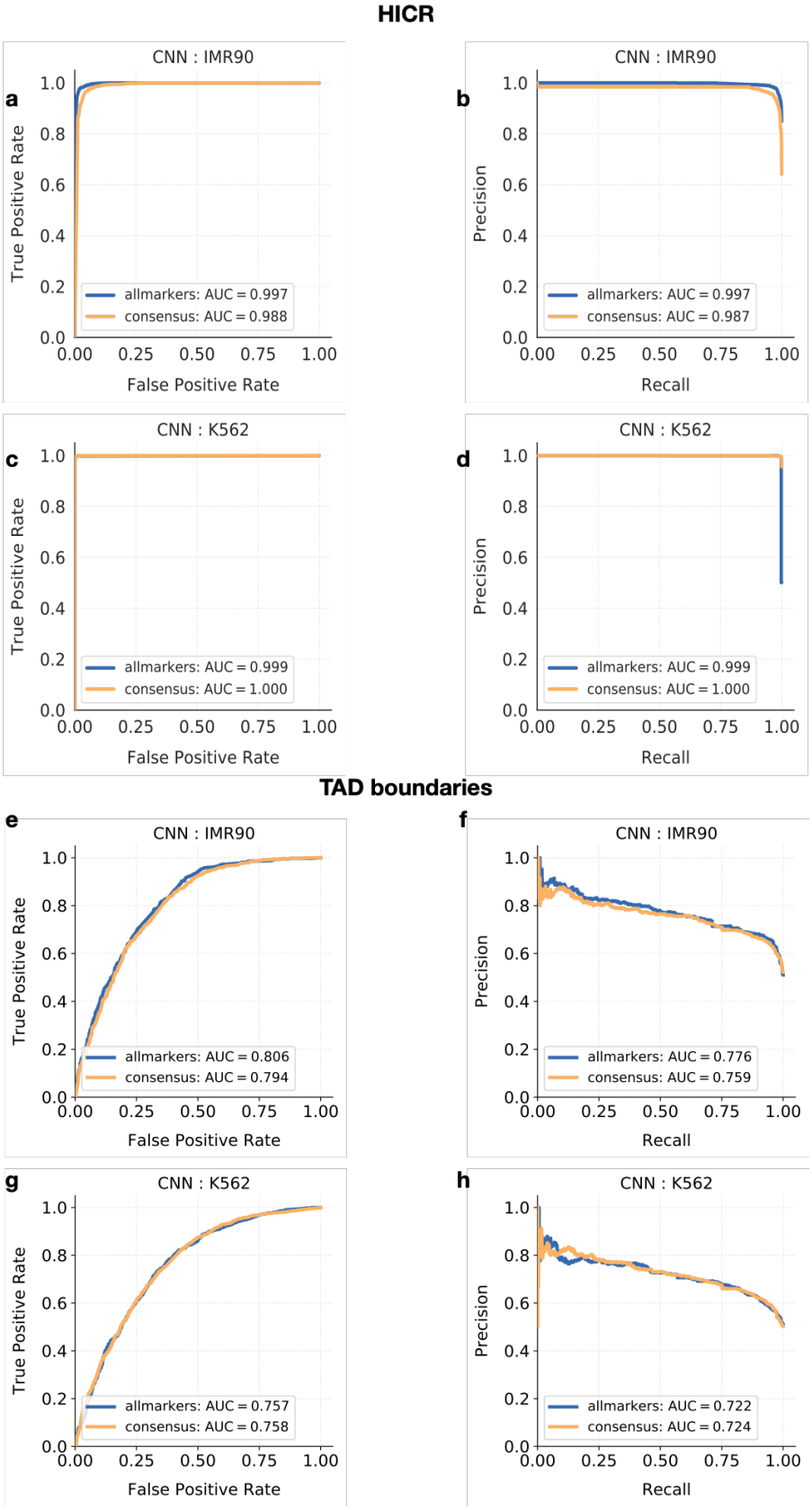

Fig. S6. CNN performance on IMR90 and K562. a,c,e,g Receiver-operating characteristic curve and **b,d,f,h** precision-recall curve for the binary classification task of predicting HICRs (**a-d**) and TAD boundaries (**e-h**) from histone mark data. Models were trained once using all available histone marks for each celltype (blue) and using only the consensus set (orange).

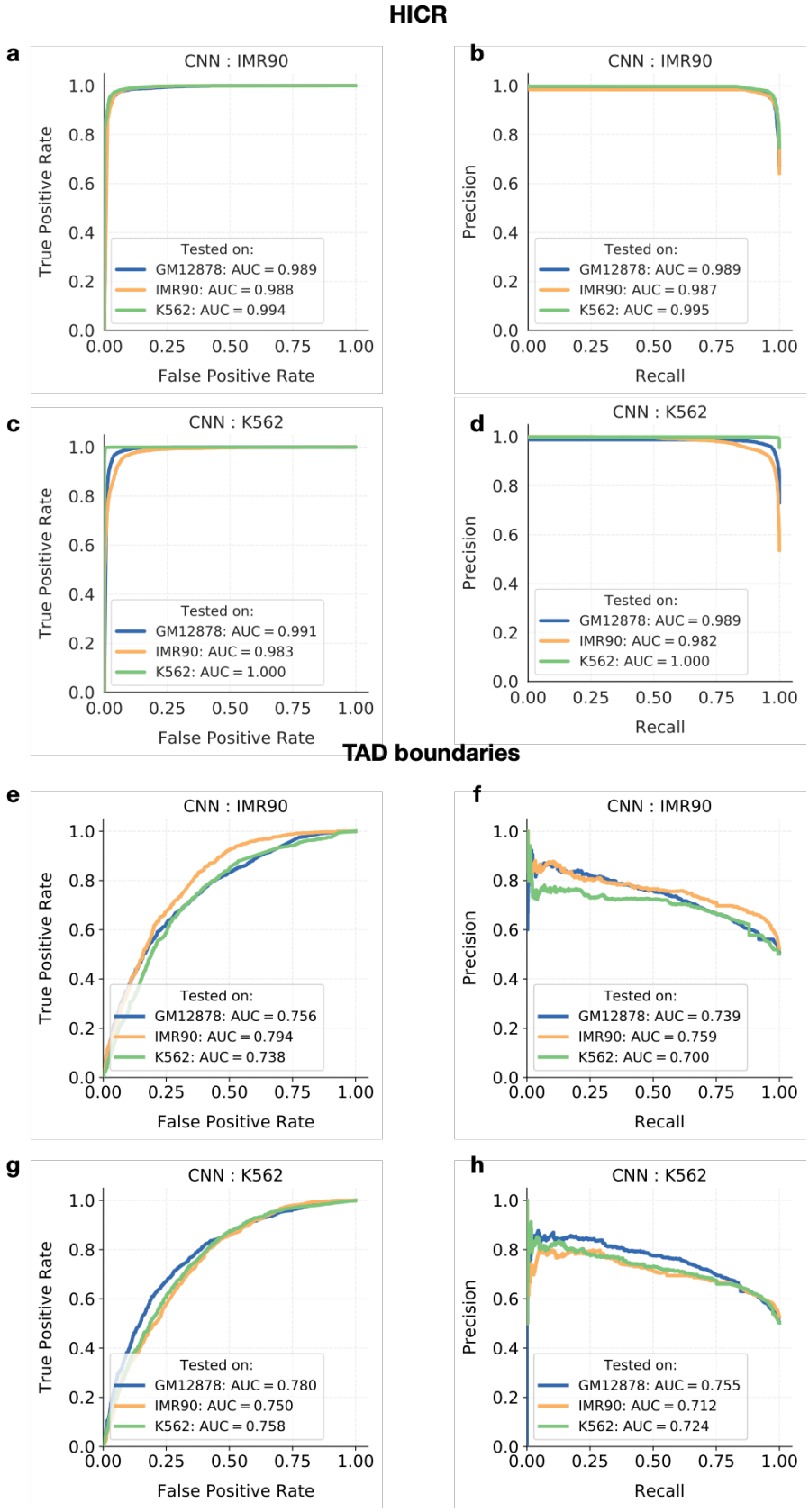

Fig. S7. Cross-cell performance on IMR90 and K562. a,c,e,g Receiver-operating characteristic curve and **b,d,f,h** precision-recall curve for the binary classification task of predicting HICRs (**a-d**) and TAD boundaries (**e-h**) in all three celltypes from models solely trained on the respective celltype data. Models were trained using only the consensus set.

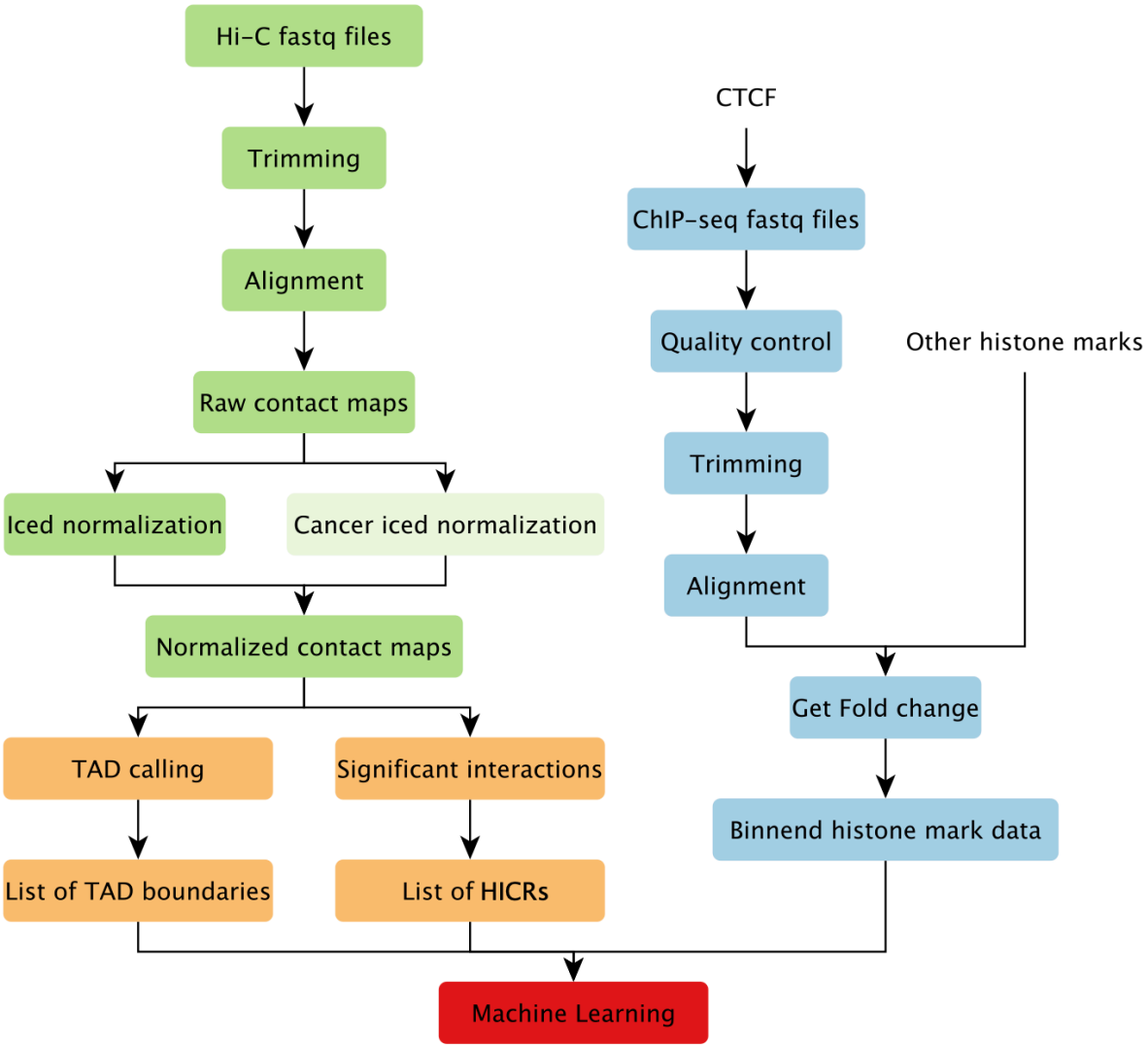

Fig. S8. Data pre-processing. In green: Hi-C paired and reads were downloaded ad fastq files. After an initial trimming step, they were aligned to the reference genome to create the raw interaction matrix. TAD calling and identification of significant interactions was performed on the normalised contact map. A list of TAD boundaries and HICRs functioned as labels for downstream supervised machine learning. In blue: If processed data was not available (CTCF), ChIP-seq fastq files were downloaded. After an initial quality control and trimming step, they were aligned to the reference genome to get fold-change values. The fold-change values were aggregated to create binned features as input for the machine learning approaches.

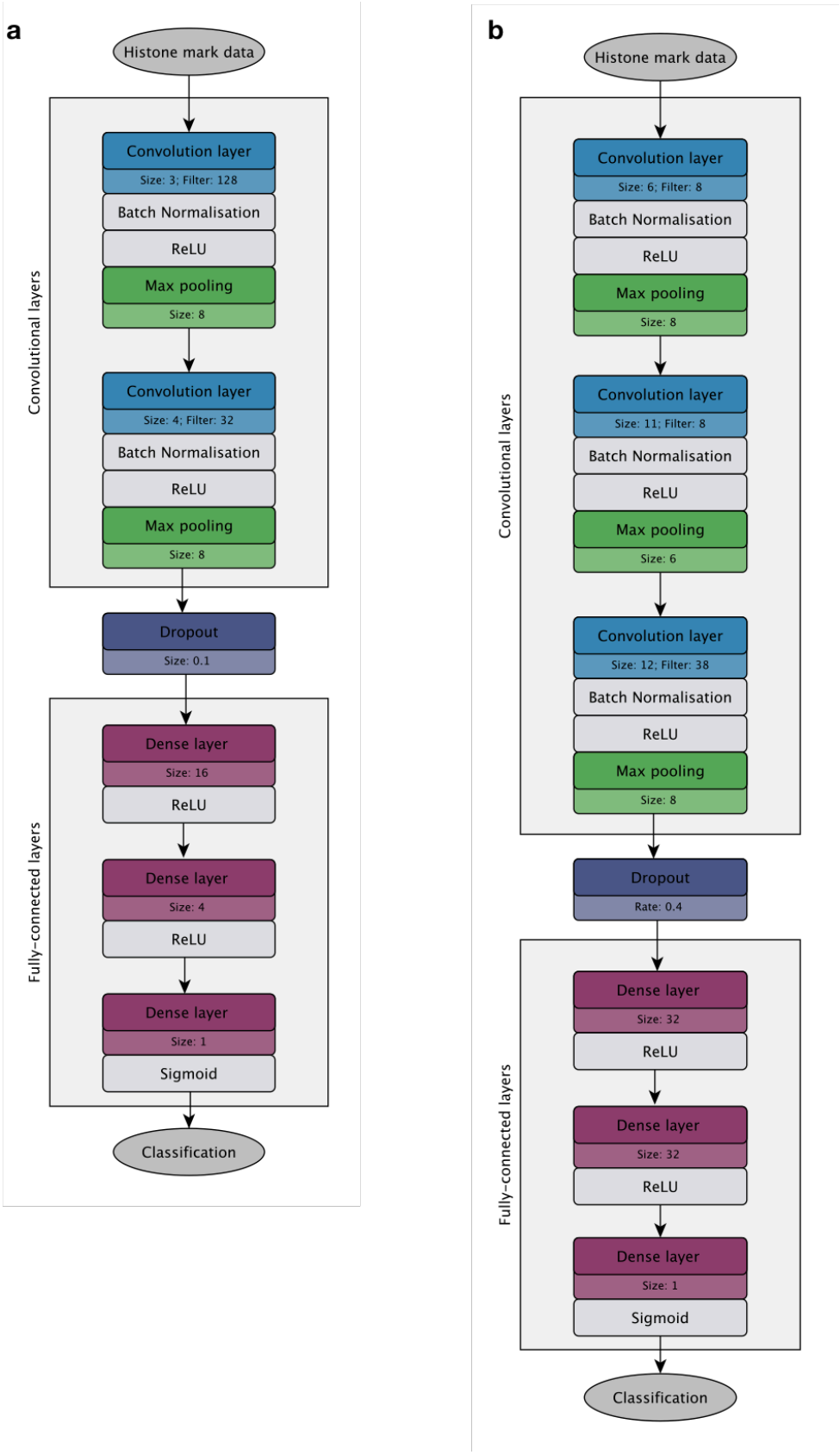

Fig. S9. Architecture of the convolutional neural networks If parameters differed from the default settings, they are indicated in the box below the layer. **a**, The CNN for HICRs consists of two convolution blocks followed by a dropout layer and two hidden fully connected layers. **b**, The CNN for TAD boundaries consists of three convolution blocks followed by a dropout layer and two hidden fully connected layers.

Tables

Table S1

Database	Celltype	HICRs		TAD boundaries	
		total number	percentage	total number	percentage
dbSUPER	GM12878	596	0.043516	51	0.008076
	IMR90	466	0.038911	77	0.014126
	K562	703	0.053701	159	0.024961
EnAtlas	GM12878	9193	0.671218	3086	0.488678
	IMR90	8534	0.712592	3544	0.650156
	K562	8252	0.630357	2955	0.463893
Enhancers_Fantom5	GM12878	7098	0.518254	3011	0.476801
	IMR90	5670	0.473447	2678	0.491286
	K562	6239	0.476587	3192	0.501099
Genehancer	GM12878	13694	0.999854	5998	0.949802
	IMR90	11947	0.997578	5227	0.958907
	K562	13088	0.999771	6076	0.953846
SEdb/Enhancer_Element	GM12878	427	0.031177	36	0.005701
	IMR90	539	0.045007	123	0.022565
	K562	658	0.050264	142	0.022292
SEdb/Super_Enhancer	GM12878	427	0.031177	36	0.005701
	IMR90	539	0.045007	123	0.022565
	K562	658	0.050264	142	0.022292
SEdb/Typical_Enhancer	GM12878	5351	0.390698	1282	0.203009
	IMR90	3620	0.302271	1256	0.230416
	K562	3635	0.277672	1338	0.210047

Table S2

Database	Celltype	HICRs		TAD boundaries	
		total number	percentage	total number	percentage
TF_clusters USCS	GM12878	13689	0.999489	6202	0.982106
	IMR90	11969	0.999415	5339	0.979453
	K562	13080	0.999160	6197	0.972841
TSS_Ensembl	GM12878	7107	0.518911	3476	0.550435
	IMR90	3986	0.332832	3339	0.612548
	K562	6991	0.534031	3554	0.557928
TSS_Fantom	GM12878	13019	0.950570	5718	0.905463
	IMR90	10763	0.898714	5014	0.919831
	K562	12253	0.935987	5793	0.909419
Ensembl_Genes	GM12878	10727	0.783221	4516	0.715123
	IMR90	7847	0.655227	4130	0.757659
	K562	9871	0.754029	4527	0.710675
Conservation	GM12878	13693	0.999781	6224	0.985590
	IMR90	11975	0.999916	5368	0.984773
	K562	13088	0.999771	6275	0.985086
CpG_Islands	GM12878	4450	0.324912	2505	0.396675
	IMR90	1933	0.161406	2398	0.439919
	K562	5072	0.387442	2505	0.393250
Ensembl_Regulatory_Build	GM12878	10088	0.736565	4180	0.661916
	IMR90	6849	0.571894	3813	0.699505
	K562	9834	0.751203	4290	0.673469
HFC_db	GM12878	5113	0.373321	1856	0.293903
	IMR90	3983	0.332582	1673	0.306916
	K562	5616	0.428997	1861	0.292151
UCSC microsattelites	GM12878	3181	0.232258	2510	0.397466
	IMR90	3024	0.252505	2151	0.394606
	K562	3009	0.229853	2498	0.392151
UCSC repeatmasker	GM12878	13693	0.999781	6270	0.992874
	IMR90	11975	0.999916	5404	0.991378
	K562	13088	0.999771	6322	0.992465

Table S3. List of available ChIP-seq datasets for each celltype and the consensus set.

	IMR90	GM12878	K562	consensus
H2AK5ac	✓			
H2AK9ac	✓			
H2BK5ac	✓			
H2BK12ac	✓			
H2BK15ac	✓			
H2BK20ac	✓			
H2BK120ac	✓			
H3K4ac	✓			
H3K4me1	✓	✓	✓	✓
H3K4me2	✓	✓	✓	✓
H3K4me3	✓	✓	✓	✓
H3K9ac	✓	✓	✓	✓
H3K9me1	✓		✓	
H3K9me3	✓	✓	✓	✓
H3K14ac	✓			
H3K18ac	✓			
H3K23ac	✓			
H3K27ac	✓	✓	✓	✓
H3K27me3	✓	✓	✓	✓
H3K36me3	✓	✓	✓	✓
H3K56ac	✓			
H3K79me1	✓			
H3K79me2	✓	✓	✓	✓
H4K5ac	✓			
H4K8ac	✓			
H4K20me1	✓	✓	✓	✓
H4K91ac	✓			
CTCF	✓	✓	✓	✓
DNase		✓	✓	
H2A.Z		✓	✓	

Table S4. Logistic Regression -Hyperparameter space and optimal parameters

parameter	space	optimal parameter	
		HICR	TAD boundary
penalty	[none , L2]	L2	L2
C	loguniform: $0.001 - 10$	3.762	0.460
solver	['lbfgs', 'saga']	'saga'	'lbfgs'
max_iter	[100, 150, 200, 250, 300]	100	100

Table S5. XGBoost: Hyperparameter space and optimal parameters

parameter	space	optimal parameter	
		HICR	TAD boundary
max_depth	[3, 2]	3	3
n_estimator	300, 310, 320, . . . , 1200	560	870
subsample	[0.75, 0.5, 0.25]	0.5	0.75
colsample_bytree	[0.75, 0.5, 0.25, 0.125]	0.75	0.75
learning_rate	loguniform: 0.00001 - 0.001	0.0496	0.0496

Table S6. CNN: Hyperparameter space and optimal parameters

parameter	space	Optimal Parameters	
		HICR	TAD boundary
filter	[8, 16, 32, 64, 128, 256]	(128, 32)	(8, 8, 32)
kernel size	2, 3, . . . , 12	(3, 4)	(6, 11, 12)
pooling size	1, 2, . . . 8	(8, 8)	(8, 6, 8)
n nodes	[2, 4, 8, 16, 32]	(16, 4)	(32, 32)
dropout	uniform: 0 - 0.5	0.046	0.392
cnn layers	[1, 2, (3)]	2	3
dense layers	[1, 2, 3]	2	2
batch_size	[32, 64, 128, 256]	256	32
epochs	10 - 20	14	17
learning_rate	loguniform: 0.00001 - 0.001	0.0083	0.0196

Table S7. HICRs: Different metrics for evaluation of Logistic Regression model.

celltype	markers	Acc.	Recall	Precision	F1	ROC AUC	PR AUC
GM12878	allmarkers	0.951	0.930	0.966	0.947	0.990	0.990
	consensus	0.946	0.920	0.964	0.942	0.987	0.987
IMR90	allmarkers	0.951	0.947	0.947	0.947	0.990	0.988
	consensus	0.925	0.907	0.931	0.919	0.979	0.976
K562	allmarkers	0.984	0.981	0.988	0.984	0.999	0.998
	consensus	0.981	0.975	0.988	0.981	0.998	0.997

Table S8. TAD boundaries: Different metrics for evaluation of Logistic Regression model.

celltype	markers	Acc.	Recall	Precision	F1	ROC AUC	PR AUC
GM12878	allmarkers	0.689	0.670	0.685	0.678	0.754	0.686
	consensus	0.687	0.663	0.685	0.674	0.750	0.683
IMR90	allmarkers	0.704	0.717	0.691	0.704	0.764	0.698
	consensus	0.699	0.703	0.690	0.696	0.754	0.690
K562	allmarkers	0.681	0.668	0.697	0.682	0.740	0.705
	consensus	0.677	0.662	0.693	0.677	0.738	0.704